# Human-machine collaboration: Ordering mechanism of rank-2 spin liquid on breathing pyrochlore lattice

Nicolas Sadoune,[1,2] Ke Liu,[1,2,3,4] Han Yan,[5,6,7,8] Ludovic D. C. Jaubert,[9] Nic Shannon,[5] and Lode Pollet[1,2]

[1]*Arnold Sommerfeld Center for Theoretical Physics, LMU Munich, Theresienstr. 37, 80333 München, Germany*

[2]*Munich Center for Quantum Science and Technology (MCQST), 80799 München, Germany*

[3]*Hefei National Research Center for Physical Sciences at the Microscale and School of Physical Sciences, University of Science and Technology of China, Hefei 230026, China*

[4]*Shanghai Research Center for Quantum Science and CAS Center for Excellence in Quantum Information and Quantum Physics, University of Science and Technology of China, Shanghai 201315, China*

[5]*Theory of Quantum Matter Unit, Okinawa Institute of Science and Technology Graduate University, Onna-son, Okinawa 904-0412, Japan*

[6]*Institute for Solid State Physics, University of Tokyo, Kashiwa, 277-8581 Chiba, Japan*

[7]*Department of Physics and Astronomy, Rice University, Houston, Texas 77005, USA*

[8]*Smalley-Curl Institute, Rice University, Houston, Texas 77005, USA*

[9]*CNRS, Université de Bordeaux, LOMA, UMR 5798, 33400 Talence, France*

(Received 16 February 2024; accepted 19 May 2025; published 14 July 2025)

Machine-learning algorithms thrive on large data sets of good quality. Here we show that they can also excel in a typical research setting with little data of limited quality, through an interplay of insights coming from machine and human researchers. The question we address is the unsolved problem of ordering out of a spin-liquid phase described by an emergent rank-2 U(1) gauge theory, as described by H. Yan *et al.* [Phys. Rev. Lett. **124**, 127203 (2020)]. Published Monte Carlo simulations for this problem are consistent with a strong first-order phase transition, but were too noisy for the form of low-temperature order to be identified. Using a highly interpretable machine-learning approach based on a support vector machine with a tensorial kernel, we reanalyze these Monte Carlo data, gaining new information about the form of order that could in turn be interpreted by traditionally trained physicists. We find that the low-temperature ordered phase is a form of magnetic order analogous to a smectic liquid crystal. This arises due to a subtle thermal order-by-disorder mechanism, that can be understood from the fluctuations of the tensor electric field of the parent rank-2 gauge theory. These results were obtained by a back-and-forth process which closely resembles a collaboration between human researchers and machines. We argue that this "collaborative" approach may provide a blueprint for solving other problems that have not yielded to human insights alone.

DOI: 10.1103/c6z1-wh6l

## I. INTRODUCTION

The past decade has seen great advances in the application of machine-learning techniques to complex data sets. Large language models, trained on hundreds of billions of words of text, are now capable of generating humanlike text, and correctly answering examinations in many different subjects [1–3]. This "generative AI" approach has undoubtedly generated great excitement, and such tools have found diverse uses as aids to constructing images, legal documents, and even computer code, based on existing models. However, it is less clear what the impact of machine learning will be in fundamental research where, by definition, there are no existing models to follow. The fact that 21st-century science produces vast quantities of data, coming both from experiment and simulation, suggests that is also ripe for the application of machine learning. But as yet, no simple template has emerged for how researchers confronted with intractable problems can best use machine-learning tools to unlock them.

Modern condensed matter physics is notable as a source of both novel physical phenomena and large data sets. A particularly rich vein of new physics, and big data, is found in frustrated magnets. Magnetic materials typically undergo a phase transition into an ordered state at low temperatures, with the type of order achieved characterized by the symmetries it breaks [4]. In frustrated magnets, competition between different interactions eliminates conventional magnetic order, leading to a dizzying array of new phenomena, including spin liquids [5,6], whose excitations include emergent magnetic monopoles [7,8], emergent photons [8–11], and Majorana fermions [12,13], as well as exotic, unconventional forms of magnetic order [14]. The effort to understand these phenomena rests heavily on the large data sets produced by inelastic neutron scattering (INS) experiments, and by Monte Carlo simulation of microscopic models. And this collision between complex science and big data makes frustrated magnetism a natural candidate for the application of machine learning.

*Published by the American Physical Society under the terms of the Creative Commons Attribution 4.0 International license. Further distribution of this work must maintain attribution to the author(s) and the published article's title, journal citation, and DOI.*

A wide variety of different machine-learning techniques have already been applied to frustrated magnets, and closely related problems [15–37]. In some cases, where it can be trained without prior assumptions, machine learning has proved capable of performing a role similar to a human researcher. This is particularly true of the analysis of Monte Carlo simulation, where interpretable forms of machine learning have proved capable of classifying different magnetic phases "from scratch." A number of different calculations of this type have been carried out for frustrated models [15,23,24,26,29,36], successfully reproducing complicated phase diagrams for systems with emergent gauge symmetry [24,29], and even of identifying magnetically ordered phases not previously anticipated by other means [30]. Meanwhile, on the experimental side, machine-learning techniques have been successfully combined with simulations of dynamics, to extract the parameters of a microscopic models from inelastic neutron scattering experiments [37].

One factor which all of these success stories have in common is access to high-quality data, of the kind which is not always available at the frontiers of understanding. Precisely because of the wide range of possible outcomes, numerical simulations of frustrated magnets are notoriously difficult to perform, showing a strong tendency to fall out of equilibrium at low temperatures [38–45]. Even where simulations converge, results can still be challenging to interpret [46–52]. As a consequence, many interesting questions about the emergent phenomena found in frustrated models at low temperature remain out of reach. Can machine learning contribute in this case? And if so, how?

With these questions in mind, this paper has two objectives: first, to solve a clearly motivated physics problem, in an active field of research, which has so far proved intractable by conventional methods, in part because of the failure of simulations to converge. And, second, to show how this solution becomes possible through an interaction between human and machine learning.

The problem we consider is an archetypical "hard problem" in frustrated magnetism: identifying the new phase which arises upon cooling from a spin liquid described by an emergent rank-2 gauge field, in a model motivated by breathing pyrochlore magnets [53–55]. The magnetic moments in this spin liquid are disordered, but very far from random, satisfying a local constraint which takes the form of a generalized Gauss' law [56–58]. This Gauss' law, which is expressed in terms of tensor fields, implies an emergent gauge symmetry, with attendant conservation laws. As a consequence excitations have "fracton" character, moving in reduced dimension [56], and characteristic power laws are found in spin correlations [53,57].

Higher-rank spin liquids are interesting as examples of novel phases of matter, but also significant because of deep connections with quantum computing [59,60], and attempts to understand quantum gravity [61–66]. Unfortunately, higher-rank spin liquids are also intrinsically challenging to simulate since they are built from an exponentially large number of degenerate spin configurations, which are not connected by the updates used in conventional MC simulation. And this challenge gets even greater where the spin liquid undergoes a low-temperature transition into a phase in which this degeneracy is wholly or partially lifted, splitting the ground-state manifold into disjoint pieces.

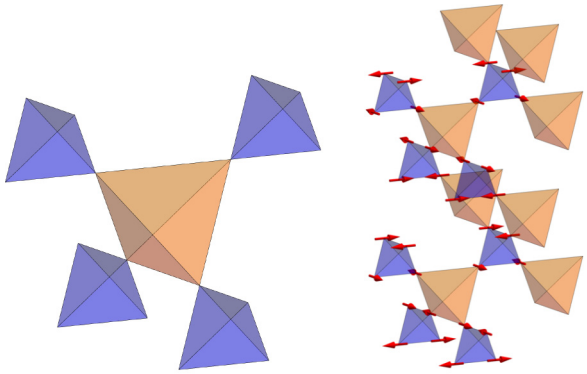



FIG. 1. Breathing pyrochlore lattice, and example of ground state found with the aid of machine-learning (AI) techniques. (a) 16-site cubic unit cell of the breathing pyrochlore lattice, with face-centered-cubic (fcc) symmetry. Four small $A$-sublattice tetrahedra, and one large $B$-sublattce tetrahedron, are shown. (b) Example of magnetic ground state found through the use of AI. The state shown has a 32-site unit cell, and is associated with wave vector $\mathbf{q} = W$.

In earlier work by Yan *et al.* [53], a rank-2 U(1) spin liquid was identified in classical Monte Carlo (MC) simulation of a model

$$\mathcal{H} = J \sum_{\langle ij \rangle} \boldsymbol{S}_i \cdot \boldsymbol{S}_j + D \sum_{\langle ij \rangle \in A} \hat{\boldsymbol{d}}_{ij} \cdot (\boldsymbol{S}_i \times \boldsymbol{S}_j) \tag{1}$$

in which antiferromagnetic (AF) Heisenberg exchange $J$ competes with Dzyaloshinskii-Moriya (DM) interactions $D$, on a breathing pyrochlore lattice (Fig. 1). Traditional methods, based on the calculation of structure factors, were used to identify correlations characteristic of rank-2 spin liquid at temperatures $T_c \lesssim 0.01\ J$ (Fig. 2). On further cooling, the model exhibited a transition into an ordered state at $T \approx 0.001$ J. However, despite the application of a combination of powerful MC techniques (heat-bath, parallel-tempering, and overrelaxation techniques), it proved impossible to thermalize simulations at these temperatures well enough to identify the form of order realized [Fig. 3(a)]. Both the extreme difficulty of simulating this phase transition and the novelty of the physics involved make it an interesting test case for the application of machine learning.

Here we revisit those simulations, and show what is gained by analyzing data using a variant of a support vector machine with tensorial kernel (TKSVM) [23,24,26]. This highly interpretable form of machine learning is employed without prior training or supervision. Through a step-by-step iteration of the insights derived from human and machine learning, we are able to successfully identify both the form of order, and the mechanism through which it occurs. Ultimately, this permits us to obtain well-equilibrated MC simulation results for the ordered phase, by initializing simulations from one of the spin configurations identified by the TKSVM, with results shown in Fig. 3.

The outcomes are twofold: First, we are able to characterize the phase found at low temperatures as an ordered

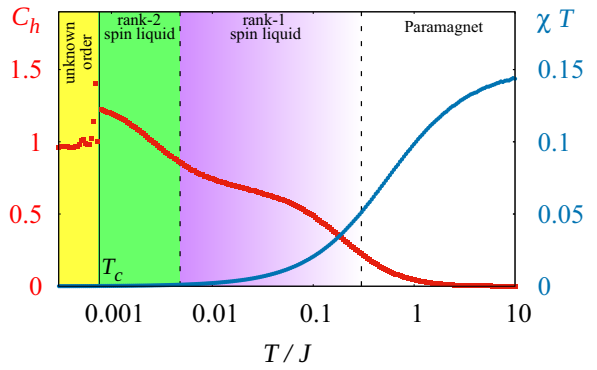



FIG. 2. Detail of phase diagram for parameters considered in this article, showing how a rank-2 spin liquid undergoes a phase transition into an unidentified form of magnetic order at low temperature. Successive crossovers from a high-temperature paramagnet into rank-1 and rank-2 spin liquids are accompanied by steep rises in the heat capacity $C_h$, with a corresponding evolution of the magnetic susceptibility $\chi$, here plotted as $\chi \times T$. The ordering transition is visible as a sharp discontinuity in $C_h$ for $T \approx 0.001$ J. Results are taken from classical Monte Carlo (MC) simulations of Eq. (1) for a cluster of linear dimension $L = 8$ ($N = 8192$ sites), with parameters (31), as described in Secs. II A and III.

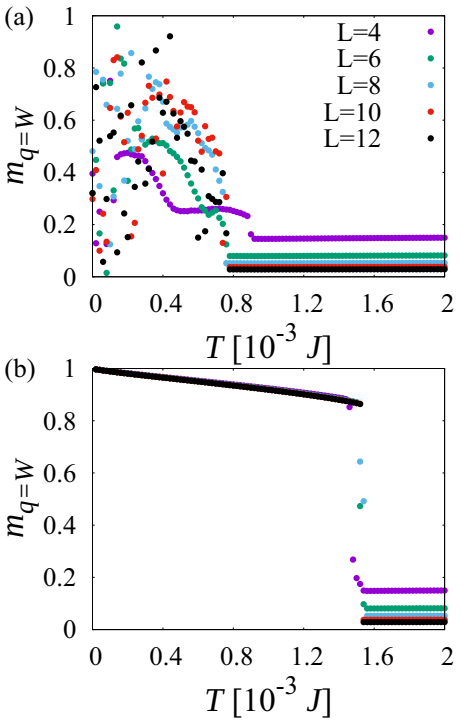



FIG. 3. Classical Monte Carlo (MC) simulation results for breathing pyrochlore model before and after input from machine learning (AI). (a) MC results before input from AI, as discussed by Yan *et al.* [53]. The staggered magnetization $m_{\mathbf{q}}$, at wave vector $\mathbf{q} = W$, shows signs of a phase transition into an ordered state for $T \sim 10^{-3}$ J. However simulations at these temperatures are too poorly converged for the form of order to be identified. (b) MC after input from AI, as described in Sec. V. Once simulations are initialized within the states identified by AI, a clear first-order phase can be identified at $T_c \approx 1.5 \times 10^{-3}$ J. Simulations were carried out for the model (1), for clusters with linear dimension $L \in \{4, 6, 8, 10, 12\}$, with parameters (31), as described in Sec. III. Wave vector $\mathbf{q} = W$ corresponds to $[1\frac{1}{2}0]$ and symmetry equivalents.

phase which breaks spin-rotation symmetry through both dipolar and quadrupolar order parameters. This phase is entropically selected from a much larger set of degenerate spin configurations, and can be identified with fluctuations of the electric field within the rank-2 spin liquid (defined in Sec. II). We find that the states found at low temperature form a subextensive manifold, responsible for the quadrupolar order. The highest-symmetry state within this manifold, illustrated in Fig. 1(b), has a 32-site unit cell. This state has a finite staggered magnetization at $\mathbf{q} = W$ [cf. Fig. 3(b)].

Second, we gain insight into the process through which these results were obtained, a back-and-forth dialog between human and machine insights. We argue that this can best be characterized as "collaboration," in which neither human nor machine plays a dominant role, suggesting one possible paradigm for the solution of other difficult problems.

The remainder of the article is structured as follows: In Sec. II we provide details of the model studied and parameters used in simulation, and review the theory of the rank-2 U(1) spin liquid developed in [53]. In Sec. III we summarize the MC results obtained without input from machine learning, showing how simulations fall out of equilibrium for $T \lesssim 10^{-3}$ J, at the phase transition from a rank-2 spin liquid into an unidentified form of magnetic order. In Sec. IV we describe application of a support vector machine with tensorial kernel (TKSVM) to MC data, and summarize results found for kernels of rank 1 and rank 2. Using this information, we reconstruct the spin configurations found on $A$- and $B$-sublattice tetrahedra for $T < T_c$. In Sec. V we revisit MC simulations in the light of what we have learned from the TKSVM, quenching from an ordered state with 32-site unit cell, built from $A$- and $B$-sublattice tetrahedra with configurations identified in Sec. IV. Simulations then converge, providing a new estimate $T_c \approx 1.5 \times 10^{-3}$ J. In Sec. VI we explore the further implications of the correlations identified in Sec. IV, identifying an emergent $\mathbb{Z}_2$ symmetry, associated with flipping an entire plane of spins, and the associated manifold of $2^L$ degenerate ground states. In Sec. VII we reexpress what we have learned about spin configurations for $T < T_c$ in the language of irreps of $T_d$, providing a new interpretation of the $\mathbb{Z}_2$ symmetry identified in Sec. VI. We conclude in Sec. VIII with a summary of results, and reflect on the interplay of human and machine insights which made it possible to identify the form of ground-state order in this model. We identify a number of other problems which might be susceptible to a similar approach.

Further technical details are provided in three Appendixes. In Appendix A we summarize the conventions used in defining the breathing pyrochlore lattice and irreps of $T_d$. In Appendix B we provide a concise overview of the TKSVM approach used to analyze MC data. Finally, in Appendix C we discuss the way in which decision functions obtained in TKSVM can be interpreted in terms of spin correlations.

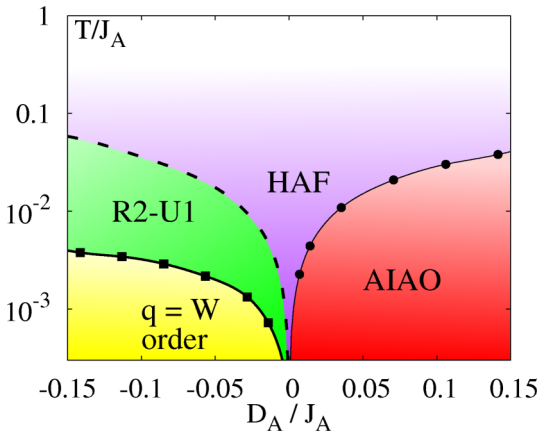



FIG. 4. Finite-temperature phase diagram of the breathing pyrochlore model, Eq. (1), as a function of DM interaction $D$, reproduced from [53]. The crossover between the R2-U1 spin liquid, and the rank-1 spin liquid (HAF), is shown with a dashed line. The thin solid line indicates a continuous transition into all-in–all-out order (AIAO). The unidentified phase at low temperatures is labeled $\mathbf{q} = W$ order, and is separated from the R2-U1 spin by a discontinuous phase transition. Results are taken from MC simulation of Eq. (1), as described in the text.

## II. BREATHING PYROCHLORE MODEL AND KNOWN PHASES

### A. Model

The model we consider is a classical Heisenberg antiferromagnet on the breathing pyrochlore lattice, with competing Dzyaloshinskii-Moriya (DM) interactions on $A$-sublattice tetrahedra,

$$\mathcal{H} = J \sum_{\langle ij \rangle} \boldsymbol{S}_i \cdot \boldsymbol{S}_j + D \sum_{\langle ij \rangle \in A} \hat{\boldsymbol{d}}_{ij} \cdot (\boldsymbol{S}_i \times \boldsymbol{S}_j),$$

previously defined in Eq. (1), and illustrated in Fig. 1. The position of lattice sites, and orientation of the DM vectors $\hat{\boldsymbol{d}}_{ij}$, are specified in Appendix A. This model was studied by Yan *et al.* [53], as a route to realizing an exotic rank-2 U(1) spin liquid, reviewed below.

The parameters $J > 0, D < 0$ are also applicable to $A$-sublattice tetrahedra within the breathing pyrochlore magnet $Ba_3Yb_2Zn_5O_{11}$ [67–69]. However, in this case the interactions on the $B$-sublattice tetrahedra are too small to accurately characterize.

In what follows we briefly recap what is already known about the different ordered and spin-liquid phases supported by this model, as summarized in Fig. 4.

### B. Ordered ground state for $D > 0$

For positive $D > 0$, the ground state is a simple all-in–all-out ordered phase [70–72]. This state is achieved through a first-order phase transition, denoted with a solid line in Fig. 4.

### C. Rank-1 spin liquid for $D = 0$ (standard formulation)

For $J_B = J_A = J = 1$ and $D = 0$ the model reduces to a Heisenberg antiferromagnet (HAF) on the pyrochlore lattice, which provides a celebrated example of classical spin liquid [73,74]. In the large-$N$ limit [75], this spin liquid can be understood as three, independent, copies of a spin-ice-like U(1) spin liquid. We briefly review this argument below. A more extended discussion can be found in [76].

We first consider a single component of spin,

$$S_i^\alpha, \quad \alpha \in \{x, y, z\}. \tag{2}$$

Within any given tetrahedron, this contributes to the Hamiltonian as

$$\Delta\mathcal{H}_{\text{tet}}^\alpha = J \left( \sum_{i \in \text{tet}} S_i^\alpha \right)^2. \tag{3}$$

The energy associated with Eq. (3) is minimized by spin configurations satisfying an emergent Gauss' law

$$\nabla \cdot \boldsymbol{E}_i^\alpha = 0, \quad \boldsymbol{E}_i^\alpha = S_i^\alpha \hat{\boldsymbol{z}}_i, \tag{4}$$

where $\{\hat{\boldsymbol{z}}_i\}$ is the local unit vector on site $i$, pointing from one center of a tetrahedron to another. The emergent electric field $\boldsymbol{E}_i^\alpha$ is defined on each site $i$ of the pyrochlore lattice or, equivalently, each link of the dual diamond lattice [76]. Note that here, although $\alpha$ labels the component of spin $\boldsymbol{S}$, but on $\boldsymbol{E}$ it labels the "copy" of electric field. There are three copies of electric field, each obeying its own Gauss' law.

Within a "large-$N$" limit, where the number of spin components $N \to \infty$, we can soften the spin-length constraint

$$|\mathbf{S}_i| = 1 \; \forall \; i \in \{1 \ldots N_{\text{sites}}\} \to \frac{1}{N_{\text{sites}}} \left| \sum_{i=1}^{N_{\text{sites}}} \mathbf{S}_i \right| = 1. \tag{5}$$

Under this assumption, the three different components of spin $\{S^x, S^y, S^z\}$ fluctuate independently, and Eq. (4) defines three independent copies of a Gauss' law. It follows that we can introduce three, independent, fields $\mathbf{A}^\alpha$ with vector (rank-1) character, such that

$$\boldsymbol{E}_i^\alpha = \nabla \times \mathbf{A}^\alpha, \tag{6}$$

and physical properties of the system invariant under the three, independent, U(1) gauge transformations

$$\mathbf{A}^\alpha \to \mathbf{A}^\alpha + \nabla \theta^\alpha. \tag{7}$$

For this reason, the spin liquid found in the Heisenberg AF on the pyrochlore lattice is commonly known as a

$$\text{U(1)} \times \text{U(1)} \times \text{U(1)}$$

spin liquid, with each $\theta^\alpha$ defining an independent U(1) gauge degree of freedom [77]. In what follows, we shall refer to the spin liquid found for $D = 0$ as the a *rank-1* U(1) spin liquid, to distinguish it from the *rank-2* U(1) spin liquid, to be introduced below.

The defining property of the rank-1 U(1) spin liquid is its Gauss' law, Eq. (4), which leads to algebraic correlation of spins, and is experimentally observable through twofold "pinch points" in the equal-time structure factor $S(\mathbf{q})$ [76]. This spin liquid persists down to $T \to 0$ at $D = 0$, connecting smoothly with the ground-state manifold defined by

$$\Delta\mathcal{H}_{\text{tet}}^\alpha = 0 \quad \forall \quad \alpha \in \{x, y, z\}. \tag{8}$$

For finite values of $|D| \ll J$, the rank-1 spin liquid survives at finite temperature, thanks to the extensive entropy,

TABLE I. Irreps of the symmetry group of isolated tetrahedron $T_d$. The convention for labeling sites is defined in Appendix A.

| Irrep | Definition in terms of spin components |
|---|---|
| $m_{\mathsf{A}_2}$ | $\frac{1}{2\sqrt{3}}\left(S_0^x+S_0^y+S_0^z+S_1^x-S_1^y-S_1^z-S_2^x+S_2^y-S_2^z-S_3^x-S_3^y+S_3^z\right)$ |
| $\mathbf{m}_{\mathsf{E}}$ | $\begin{pmatrix}\frac{1}{2\sqrt{6}}\left(-2S_0^x+S_0^y+S_0^z-2S_1^x-S_1^y-S_1^z+2S_2^x+S_2^y-S_2^z+2S_3^x-S_3^y+S_3^z\right)\\ \frac{1}{2\sqrt{2}}\left(-S_0^y+S_0^z+S_1^y-S_1^z-S_2^y-S_2^z+S_3^y+S_3^z\right)\end{pmatrix}$ |
| $\mathbf{m}_{\mathsf{T}_{1+}}$ | $\begin{pmatrix}\frac{1}{2}\left(S_0^x+S_1^x+S_2^x+S_3^x\right)\\ \frac{1}{2}\left(S_0^y+S_1^y+S_2^y+S_3^y\right)\\ \frac{1}{2}\left(S_0^z+S_1^z+S_2^z+S_3^z\right)\end{pmatrix}$ |
| $\mathbf{m}_{\mathsf{T}_{1-}}$ | $\begin{pmatrix}\frac{-1}{2\sqrt{2}}\left(S_0^y+S_0^z-S_1^y-S_1^z-S_2^y+S_2^z+S_3^y-S_3^z\right)\\ \frac{-1}{2\sqrt{2}}\left(S_0^x+S_0^z-S_1^x+S_1^z-S_2^x-S_2^z+S_3^x-S_3^z\right)\\ \frac{-1}{2\sqrt{2}}\left(S_0^x+S_0^y-S_1^x+S_1^y+S_2^x-S_2^y-S_3^x-S_3^y\right)\end{pmatrix}$ |
| $\mathbf{m}_{\mathsf{T}_2}$ | $\begin{pmatrix}\frac{1}{2\sqrt{2}}\left(-S_0^y+S_0^z+S_1^y-S_1^z+S_2^y+S_2^z-S_3^y-S_3^z\right)\\ \frac{1}{2\sqrt{2}}\left(S_0^x-S_0^z-S_1^x-S_1^z-S_2^x+S_2^z+S_3^x+S_3^z\right)\\ \frac{1}{2\sqrt{2}}\left(-S_0^x+S_0^y+S_1^x+S_1^y-S_2^x-S_2^y+S_3^x-S_3^y\right)\end{pmatrix}$ |

before crossing over to a conventional paramagnet for $T \gg J$ (Fig. 4).

### D. Rank-1 spin liquid for $D = 0$ (tensor formulation)

It is possible to formulate the rank-1 U(1) spin liquid described above as a special case of a more general rank-2 tensor theory. In what follows we review this approach, as preliminary to describing the rank-2 spin liquid found for $D < 0$. Further details can be found in [53,78–81].

We start with the observation that it is possible to combine the three vector fields $\boldsymbol{E}^\alpha$ into a single tensor field

$$E^{\mathrm{HAF}}_{\alpha\beta} = \begin{bmatrix}(E^x)_x, (E^x)_y, (E^x)_z\\ (E^y)_x, (E^y)_y, (E^y)_z\\ (E^z)_x, (E^z)_y, (E^z)_z\end{bmatrix}. \tag{9}$$

Doing so, the three Gauss' laws, Eq. (4), can be collected in a single equation

$$\partial_\beta E^{\mathrm{HAF}}_{\alpha\beta} = 0. \tag{10}$$

We can link this tensor formulation of emergent electrostatics to the energetics of the problem by transcribing the Hamiltonian (1), in terms of the irreps

$$\{\mathbf{m}_\lambda\}_{T_d} = \left\{m_{\mathsf{A}_2}, \mathbf{m}_{\mathsf{E}}, \mathbf{m}_{\mathsf{T}_{1+}}, \mathbf{m}_{\mathsf{T}_{1-}}, \mathbf{m}_{\mathsf{T}_2}\right\} \tag{11}$$

of the tetrahedral symmetry group $T_d$ (Table I), to give

$$\mathcal{H} = \frac{1}{2}\sum_{A,\lambda} a_{A,\lambda}\mathbf{m}_\lambda^2 + \frac{1}{2}\sum_{B,\lambda} a_{B,\lambda}\mathbf{m}_\lambda^2, \tag{12}$$

where the sum on $A(B)$ sum runs over all $A(B)$-sublattice tetrahedra, and the coefficients $a_{A(B),\lambda}$ are defined in Table II.

In case of the Heisenberg antiferromagnet $D = 0$, we have

$$0 < a_{\mathsf{A}_2} = a_{\mathsf{E}} = a_{\mathsf{T}_2} = a_{\mathsf{T}_{1-}} < a_{\mathsf{T}_{1+}}, \tag{13}$$

and it follows that rank-1 spin liquid contains fluctuations transforming with the irreps

$$\{m_\lambda\}_{\mathrm{HAF}} = \left\{m_{\mathsf{A}_2}, \mathbf{m}_{\mathsf{E}}, \mathbf{m}_{\mathsf{T}_1-}, \mathbf{m}_{\mathsf{T}_2}\right\} \tag{14}$$

while the irrep $\boldsymbol{m}_{\mathsf{T}_{1+}}$ describes excitations with finite charge.

Since the spin configurations within the rank-1 spin liquid are characterized by the irreps $\{m_\lambda\}_{\mathrm{HAF}}$, it must be possible to decompose the emergent electric field $\boldsymbol{E}^{\mathrm{HAF}}$ [Eq. (15)] in terms of the same set of irreps. Following [53,78,79], we write

$$\boldsymbol{E}^{\mathrm{HAF}} = \boldsymbol{E}^{\mathrm{HAF}}_{\mathrm{sym}} + \boldsymbol{E}^{\mathrm{HAF}}_{\mathrm{antisym}} + \boldsymbol{E}^{\mathrm{HAF}}_{\mathrm{trace}}, \tag{15}$$

where we have decomposed the tensor $\boldsymbol{E}^{\mathrm{HAF}}$ into its symmetric component

$$\boldsymbol{E}^{\mathrm{HAF}}_{\mathrm{sym}} = \begin{bmatrix}\frac{2}{\sqrt{3}}m^1_{\mathsf{E}} & m^z_{\mathsf{T}_{1-}} & m^y_{\mathsf{T}_{1-}}\\ m^z_{\mathsf{T}_{1-}} & -\frac{1}{\sqrt{3}}m^1_{\mathsf{E}} - m^2_{\mathsf{E}} & m^x_{\mathsf{T}_{1-}}\\ m^y_{\mathsf{T}_{1-}} & m^x_{\mathsf{T}_{1-}} & -\frac{1}{\sqrt{3}}m^1_{\mathsf{E}} + m^2_{\mathsf{E}}\end{bmatrix}, \tag{16}$$

antisymmetric component

$$\left(E^{\mathrm{HAF}}_{\mathrm{antisym}}\right)_{ij} = -\epsilon_{ijk}m^k_{\mathsf{T}_2}, \tag{17}$$

and trace

$$\left(E^{\mathrm{HAF}}_{\mathrm{trace}}\right)_{ij} = -\delta_{ij}\sqrt{\frac{2}{3}}m_{\mathsf{A}_2}. \tag{18}$$

Spatial derivative of the irreps contributing to $\boldsymbol{E}^{\mathrm{HAF}}$ are linked through the requirement of the continuity of the fields

TABLE II. Coefficients $a_\lambda$ appearing in Eq. (12), expressed in terms of the parameters of the original Hamiltonian (1).

| Coefficient | Parametrization |
|---|---|
| $a_{\mathsf{A}_2,\mathrm{A}}$ | $-J - 4D/\sqrt{2}$ |
| $a_{\mathsf{T}_2,\mathrm{A}}$ | $-J - 2D/\sqrt{2}$ |
| $a_{\mathsf{T}_{1+},\mathrm{A}}$ | $3J$ |
| $a_{\mathsf{T}_{1-},\mathrm{A}}$ | $-J + 2D/\sqrt{2}$ |
| $a_{\mathsf{E},\mathrm{A}}$ | $-J + 2D/\sqrt{2}$ |
| $a_{\mathsf{A}_2,\mathrm{B}}$ | $-J$ |
| $a_{\mathsf{E},\mathrm{B}}$ | $-J$ |
| $a_{\mathsf{T}_2,\mathrm{B}}$ | $-J$ |
| $a_{\mathsf{T}_{1-},\mathrm{B}}$ | $-J$ |
| $a_{\mathsf{T}_{1+},\mathrm{B}}$ | $3J$ |

$m_\lambda$ [79]. In particular, we have only $\boldsymbol{m}_{\mathsf{T}_{1+}} = 0$ enforced by the Hamiltonian with coefficients of Eq. (13), which imposes the conditions

$$\frac{2}{\sqrt{3}}\begin{bmatrix} \partial_x m^1_{\mathsf{E}} \\ -\frac{1}{2}\partial_y m^1_{\mathsf{E}} - \frac{\sqrt{3}}{2}\partial_y m^2_{\mathsf{E}} \\ -\frac{1}{2}\partial_y m^1_{\mathsf{E}} + \frac{\sqrt{3}}{2}\partial_y m^2_{\mathsf{E}} \end{bmatrix} - \begin{bmatrix} \partial_y m^z_{\mathsf{T}_{1-}} + \partial_z m^y_{\mathsf{T}_{1-}} \\ \partial_z m^x_{\mathsf{T}_{1-}} + \partial_x m^z_{\mathsf{T}_{1-}} \\ \partial_x m^y_{\mathsf{T}_{1-}} + \partial_y m^x_{\mathsf{T}_{1-}} \end{bmatrix}$$
$$- \sqrt{\frac{2}{3}}\boldsymbol{\nabla} m_{\mathsf{A}_2} + \boldsymbol{\nabla} \times \mathbf{m}_{\mathsf{T}_2} = 0. \tag{19}$$

Once these conditions are taken into account, the field $\boldsymbol{E}^{\mathrm{HAF}}$ [Eq. (15)] satisfies the emergent Gauss' law, Eq. (10).

We finally arrive at a phenomenological Hamiltonian describing the low-energy physics of rank-1 U(1) theory (R1U1) as

$$\mathcal{H}_{\mathrm{R1U2}} \sim U \sum_{\alpha=1,2,3} (\partial_\beta E_{\alpha\beta})^2, \tag{20}$$

where $\boldsymbol{E}$ is $\boldsymbol{E}^{\mathrm{HAF}}$. We see here that the Guass's law is enforced energetically, arising from the $a_{\mathsf{T}_{1+}} \boldsymbol{m}^2_{\mathsf{T}_{1+}}$ term.

### E. Rank-2 spin liquid for $D < 0$ (microscopic)

For negative $D < 0$, the Hamiltonian (1) does not select a ordered ground state, but instead a (sub)extensive manifold of ground states, which are in turn a subset of the manifold of states associated with the rank-1 U(1) spin liquid. As a consequence, rather than undergoing a phase transition into an ordered state on cooling, as happens for $D > 0$ (Fig. 4), the rank-1 U(1) spin liquid first undergoes a crossover into a new form of spin liquid. The structure of this ground-state manifold, and the resulting intermediate spin liquid, can be deconstructed using the language of irreps, introduced above.

Considering first the $A$-sublattice tetrahedra, for $J > 0$, $D < 0$, the coefficients $a_{\mathrm{A},\lambda}$ satisfy the condition

$$a_{\mathrm{A},\mathsf{E}} = a_{\mathrm{A},\mathsf{T}_{1-}} < a_{\mathrm{A},\mathsf{A}_2},\ a_{\mathrm{A},\mathsf{T}_2},\ a_{\mathrm{A},\mathsf{T}_{1+}}, \tag{21}$$

which implies that only the fields

$$\{m_\lambda\}_{\mathsf{D}<0} = \left\{\mathbf{m}_{\mathsf{E}}, \mathbf{m}_{\mathsf{T}_{1-}}\right\} \tag{22}$$

enter into the ground state of Eq. (12). Turning to the $B$-sublattice tetrahedra, we find a simplified form of the equation of continuity Eq. (19), via

$$\frac{2}{\sqrt{3}}\begin{bmatrix} \partial_x m^1_{\mathsf{E}} \\ -\frac{1}{2}\partial_y m^1_{\mathsf{E}} - \frac{\sqrt{3}}{2}\partial_y m^2_{\mathsf{E}} \\ -\frac{1}{2}\partial_y m^1_{\mathsf{E}} + \frac{\sqrt{3}}{2}\partial_y m^2_{\mathsf{E}} \end{bmatrix} - \begin{bmatrix} \partial_y m^z_{\mathsf{T}_{1-}} + \partial_z m^y_{\mathsf{T}_{1-}} \\ \partial_z m^x_{\mathsf{T}_{1-}} + \partial_x m^z_{\mathsf{T}_{1-}} \\ \partial_x m^y_{\mathsf{T}_{1-}} + \partial_y m^x_{\mathsf{T}_{1-}} \end{bmatrix} = 0. \tag{23}$$

Eliminating fluctuations of $m_{\mathsf{T}_2}$ and $m_{\mathsf{A}_2}$ reduces the tensor electric field $\boldsymbol{E}$ to its symmetric, traceless component $\boldsymbol{E}^{\mathrm{HAF}}_{\mathrm{sym}}$ [Eq. (16)]. This symmetric, traceless, electric field satisfies a Gauss' law

$$\partial_\alpha E_{\alpha\beta} = 0 \tag{24}$$

which defines a rank-2 U(1) gauge theory [82].

### F. Rank-2 spin liquid for $D < 0$ (phenomenological)

The spin liquid defined through Eq. (24) has properties which are substantially different from the rank-1 U(1) spin liquid discussed in Sec. II C. We can gain some insight into these new properties by considering the effective Hamiltonian

$$\mathcal{H}_{\mathrm{R2U1}} \sim U \sum_\alpha (\partial_\beta E_{\alpha\beta})^2 + \delta_1 (\mathrm{Tr}\boldsymbol{E})^2 + \delta_2 \sum_{\alpha<\beta} (E_{\alpha\beta} - E_{\beta\alpha})^2, \tag{25}$$

where $U \sim J$ and $\delta_{1,2} \sim D$. In the temperature regime $T < D$, we find an emergent Gauss' law

$$\partial_\beta E^{(\mathrm{sym})}_{\alpha\beta} = 0 \tag{26}$$

in which $E^{(\mathrm{sym})}_{\alpha\beta}$ is a rank-2 tensor, with only symmetric, traceless components. Charge is now defined through a vector

$$\rho_\alpha = \partial_\beta E^{(\mathrm{sym})}_{\alpha\beta} \tag{27}$$

and subject to an extended set of conservation laws, which comprise conservation of charge

$$\int dv\, \vec{\rho} = 0, \tag{28}$$

conservation of moment of inertia

$$\int dv\, \vec{x} \times \vec{\rho} = -\int dv\, \epsilon_{\alpha\beta\gamma} E_{\beta\gamma} = 0, \tag{29}$$

and conservation of dipole moment

$$\int dv\, \vec{x} \cdot \vec{\rho} = -\int dv\, E_{\alpha\alpha} = 0. \tag{30}$$

Following [56,83], we refer to phase with these properties as a *rank-2* U(1) spin liquid. The Gauss' law (24) also has important consequences for correlations, leading to pinch points in $S(\mathbf{q})$ with a characteristic fourfold structure [53,57].

### G. Undetermined order at low temperatures

Finally, when further decreasing the temperature for $D < 0$, the rank-2 spin liquid was found to order at a temperature $T_c \sim 10^{-3}$ J [53]. However, the nature of this order could not be determined from the analysis of Monte Carlo (MC) simulation carried out in Ref. [53] because poor thermalization made it impossible to carry out finite-size scaling of results for $T < T_c$. All that could be identified were potential Bragg peaks in the spin structure factor at finite $\mathbf{q} = W$ (corners of the Brillouin zone). These results suggested the possibility of a spin order which broke the symmetries of the lattice, in coexistence (or competition) with other low-energy states, but stopped short of identifying that order.

### H. Parameters studied in this article

It is the properties of the low-temperature ordered phase for $D < 0$, unidentified in Ref. [53], which forms the main focus this article. To this end, all MC simulations were carried out for the parameter set

$$J = 1,\ D = -0.0141, \tag{31}$$

setting $k_B = 1$, and measuring temperature $T$ in units $10^{-3}$ J. In what follows, we review the status of MC simulations of the ordered phase, prior to AI input.

## III. SIMULATIONS BEFORE AI INPUT

Monte Carlo (MC) simulations of the breathing-pyorchlore model (1), for parameters (31) were carried out following procedure used in Ref. [53], for spins length $|S| = \frac{1}{2}$, in clusters of up to $N = 27\,648$ spins. The clusters considered were of cubic symmetry, with edges parallel to the (cubic) crystal axes. These clusters contained $N = 16\,L^3$ spins, where $L$ is the linear dimension of the cluster, measured relative to a cubic unit cell which contains 16 spins, illustrated in Fig. 1(a). Lattice definitions are provided in Appendix A.

Starting from a random spin configuration, the system is annealed from high temperature to a temperature $T$ during $10^6$ Monte Carlo steps, then thermalized at $T$ for another $10^6$ Monte Carlo steps, and finally data are collected for statistical averaging during $10^7$ MC steps. Each MC step is made of $N$ single-spin-flip updates via the rejectionless heat-bath algorithm and five overrelaxation updates sweeping through the entire lattice. Overrelaxation is a microcanonical update with spin rotation around the local molecular field for each spin; we include both $\pi$ rotations (the largest one) and random ones. Every 100 MC steps, there is parallel tempering between neighboring temperatures (126 temperatures in parallel between $T = 0$ and $0.0025\,J$). These simulation parameters are typically one order of magnitude longer in time and bigger in system size than what is usually necessary to completely characterize a typical phase transition in a frustrated magnet (see, e.g., the simulation parameters in Ref. [84]). Nonetheless, we see in Fig. 5 that while it is possible to spot the presence of long-range order, we cannot properly thermalize the magnetic order at very low temperatures. As a consequence, it is unclear if the order with Bragg peaks at $\mathbf{q} = W$ is really (part of) the ground state and if it coexists, or not, with other phases.

The reasons for this issue are multiple. On a fundamental level, our problem is the ordering mechanism arising upon cooling from a higher-rank gauge field. As was shown in Ref. [53], the rank-2 gauge field itself comes out of a rank-1 gauge field with a broader phase-space manifold, namely, the Coulomb spin liquid of the Heisenberg antiferromagnet on pyrochlore. It is the DM term on $A$ tetrahedra in Eq. (1) that selects the rank-2 gauge field. This means that the ordered phase we are investigating is separated from paramagnetic fluctuations by *two* successive crossovers into more and more constrained configurational manifolds (see Fig. 2). Monte Carlo simulations are thus particularly constrained in phase space around $T_c$ and can easily be trapped in local free-energy minima.

This is where parallel tempering would usually help, by shuffling spin configurations across temperatures. But here the issue is not only that the transition temperature is far from paramagnetic fluctuations. The visible jumps in energy and order parameter in Figs. 5(a) and 5(c) suggest a first-order transition. This strongly hinders the efficiency of parallel tempering because the discontinuity in energy essentially prevents spin configurations from crossing the transition temperature. Hence, one cannot rely on parallel tempering to help thermalize the ordered phase. In addition, the energy jump in Fig. 5(a) is of the order of $10^{-4}$ J. Such a tiny energy selection is consistent with the double crossover mentioned above but, keeping in mind that we are at proximity of a highly degenerate spin liquid, it also suggests a competition between multiple phases that are quasidegenerate in free energy. Finally, the $\mathbf{q} = W$ Bragg peaks implies a large magnetic unit cell made of 32 sites, which is another complication in itself for the local heat-bath algorithm.

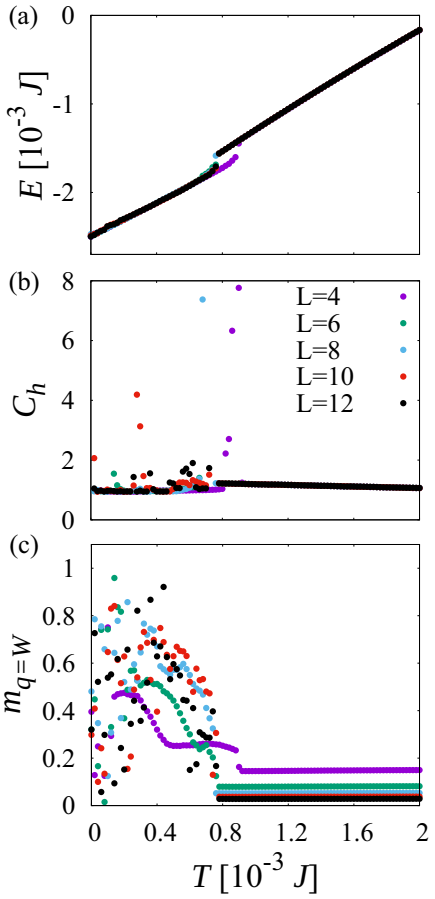



FIG. 5. Classical Monte Carlo (MC) simulation results for breathing pyrochlore model before input from machine learning, showing failure of simulations to equilibrate in the unidentified ordered phase for $T \lesssim 0.8 \times 10^{-3}$ J. (a) Energy per site $E$. (b) Heat capacity per site $C_h$. (c) Staggered magnetization $m_{\mathbf{q}}$ at the proposed ordering vector $\mathbf{q} = W$. Simulations were carried out for the model (1), for a clusters with linear dimension $L \in \{4, 6, 8, 10, 12\}$, with parameters (31), as described in Sec. III.

Our point is that, even if not necessarily systematic, we expect thermalization issues to be relatively natural consequences of higher-rank gauge fields [56,82,85,86]. Being governed by tensorial constraints and a multiplicity of conserved quantities [56], these exotic phases and dynamics are inherently complex, and it comes as to no surprise for their ordering mechanisms to be unconventional. With these caveats in mind, our goal is to show how AI is able to help us, taking advantage of what it does best: extracting useful information out of noisy and incomplete data.

## IV. MACHINE-LEARNING ALGORITHM

Our machine-learning algorithm, the tensorial kernel support vector machine (TKSVM), has been developed in

Refs. [23,24,26]. The inner workings of the TKSVM algorithm are not necessary to understand this work, as there are no algorithmic developments here, and we refer to Appendix B for a concise introduction to the method. It is, however, important to know its input requirements and output. TKSVM takes as input Monte Carlo snapshots of the spin configurations (typically 500–1000 of them) between two different data sets. Since the Hamiltonian parameters are fixed, we will compare different temperatures, in particular above and below $T_c$. It also requires as input the definition of a (typically small) cluster of sites, specified by the user. TKSVM builds on these clusters on a tensorial basis up to a predefined rank. Rank 1 can be thought of as dipolar magnetic order, rank 2 as quadrupolar order, etc. The stochastic quantities defined on this cluster are obtained by averaging spin configurations over the full lattice. This significantly reduces the data's dimension to a dependence on the size of the cluster. The output of TKSVM is the decision function used to separate data into sets with different characters. This comprises structure factors (in the term of a coefficient matrix) and a bias term. The bias, usually used to extract phase diagrams by TKSVM, plays no role in this work. The structure factors encode the order parameters squared, and can be interpreted by the user. In other words, in the (simplified) setting when the machine strips all the information differentiating two data sets down to a single scalar, the decision function encodes the local order parameter of Landau theory reflecting symmetry breaking between the two data sets. An additional strength of TKSVM is that even in the absence of order, it is able to measure local constraints hinting at a potential classical spin-liquid candidate. The extent of the locality, for both the order parameter and the spin-liquid constraint, is limited by the cluster size. As an illustrative example we refer to Ref. [24] where TKSVM successfully reproduced the phase diagram of the classical $XXZ$ model on the pyrochlore lattice computed by Taillefumier *et al.* [49]: it found, and interpreted, the ordered in-plane ferromagnetic and nematic phases, but also identified and interpreted the crossovers between the high-temperature paramagnet and spin ice, as well as the one with the Heisenberg spin liquid. Given this success and the tensorial nature of the higher-rank gauge fields, TKSVM is our method of choice to tackle our problem.

### A. Rank-1 results

Without prior knowledge of the phase, it is natural to start with the rank-1 kernel to probe potential magnetic orders well below the apparent phase transition of Fig. 5 at $T_c \approx 8 \times 10^{-4}$ J. Rank 1 means that we consider quantities which are linear combinations of the spin components of the cluster, or in other words dipolar forms of magnetic order. As the complexity of the feature vector grows linearly at rank 1 [26], we can use very large clusters consisting of multiple lattice unit cells. Provided a phase is purely magnetic and has a perfect translational symmetry, the rank-1 patterns learned with different cluster sizes should converge to a stable, regular, structure. The magnetic order parameter can then be inferred and justified *a posteriori* by measuring it in new Monte Carlo simulations.

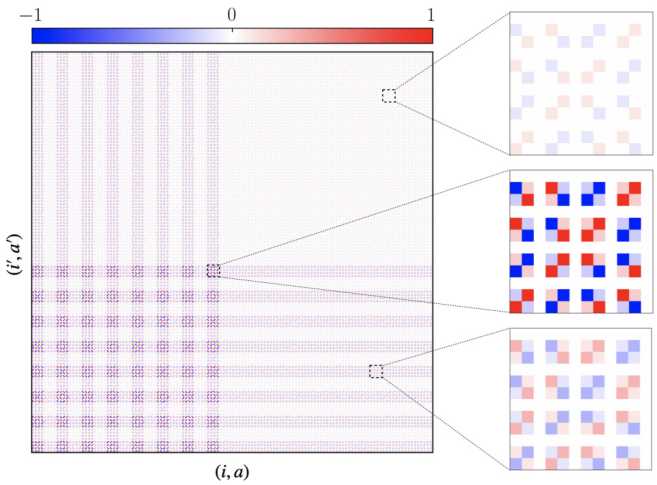



FIG. 6. Rank-1 coefficient matrix. Each pixel represents the color-scaled weight of a contraction $\langle S_i^a \rangle \langle S_{i'}^{a'} \rangle$ of rank-1 features learned by the machine. The indices $i$ and $i'$ range from 0 to 127 labeling the spins within the 128-site cluster and $a, a'$ label the spin components $x, y, z$. This $384 \times 384$ matrix is a graphical representation of the decision function for the rank-1 kernel [Eq. (B2)]. Magnification of three different spin-contraction blocks reveals their locally similar structure and different overall weight. Long-range magnetic order would have been revealed via a block pattern repeating itself across the entire matrix, which is absent here. The machine learned from spin configurations obtained by Monte Carlo simulations at $T = 4 \times 10^{-4}$ J, well below the apparent phase transition at $T_c \approx 8 \times 10^{-4}$ J in Fig. 5.

However, in the unknown phase below $T_c$, we do not observe evidence of a stable rank-1 pattern even when using very large clusters up to 128 sites (8 cubic unit cells) in Fig. 6. Instead, the learned patterns display sample-dependent irregular weights that are inconsistent with long-range dipolar order. This suggests that rank-1 magnetic orders do not reflect the correlations in the system fully, and we shall further inspect the data at rank 2 in order to confirm the presence, or not, of order below $T_c$.

### B. Rank-2 results

Rank 2 means that we consider quantities which are quadratic combinations of the spin components of the cluster, or in other words quadrupolar forms of magnetic order. The choice of the cluster at rank 2 is also guided by the lattice structure. Natural choices include a single $A$ tetrahedron, single $B$ tetrahedron, and fcc cubic unit cells of the breathing pyrochlore lattice consisting of 16 spins [see Fig. 1(a)]. We found that considering the $A$ tetrahedron and $B$ tetrahedron separately reveals all the information of the phase. After obtaining results for these clusters separately, they need to be combined to understand the structure of the ground states. Alternatively, using a fcc unit cell as a cluster directly reveals the ground-state structure, at the price of a more involved interpretation and some redundancy from the four $A$ tetrahedra contained in the cluster. For simplicity, we will present the information extracted from $A$ and $B$ tetrahedra successively.

For each of the four $A$ tetrahedra, the (sub)decision function is

$$d_A^s \sim \left(c_1^s\right)^2 + \left(c_2^s\right)^2, \tag{32}$$

where $s \in \{xy, yz, zx\}$ labels the spin plane, which spontaneously breaks the spin permutation symmetry of the Hamiltonian in Eq. (1). We stress that the spontaneous spin-plane selection is uniform over all $A$ tetrahedra, and since every spin is part of one $A$ tetrahedron, the spin-plane selection is *global*. The precise order is thus defined by two effective order parameters $c_1$ and $c_2$ that are quadratic functions of spin components,

$$\begin{aligned}
c_1^{yz} &= \tfrac{1}{16}\left[\left(S_0^y - S_1^y + S_2^z - S_3^z\right)^2 + \left(S_0^z - S_1^z - S_2^y + S_3^y\right)^2\right],\\
c_1^{xz} &= \tfrac{1}{16}\left[\left(S_0^x + S_1^z - S_2^x - S_3^z\right)^2 + \left(S_0^z - S_1^x - S_2^z + S_3^x\right)^2\right],\\
c_1^{xy} &= \tfrac{1}{16}\left[\left(S_0^x + S_1^y - S_2^y - S_3^x\right)^2 + \left(S_0^y - S_1^x + S_2^x - S_3^y\right)^2\right],
\end{aligned} \tag{33}$$

$$\begin{aligned}
c_2^{yz} &= \tfrac{2}{16}\left(S_0^y - S_1^y + S_2^z - S_3^z\right)\left(S_0^z - S_1^z - S_2^y + S_3^y\right),\\
c_2^{xz} &= \tfrac{2}{16}\left(S_0^x + S_1^z - S_2^x - S_3^z\right)\left(S_0^z - S_1^x - S_2^z + S_3^x\right),\\
c_2^{xy} &= \tfrac{2}{16}\left(S_0^x + S_1^y - S_2^y - S_3^x\right)\left(S_0^y - S_1^x + S_2^x - S_3^y\right).
\end{aligned} \tag{34}$$

As TKSVM is conceived to learn the optimal order parameters, we can reversely infer maximally ordered spin configurations by maximizing $d_A^s$. These fully ordered states are potential ground states. Note that in order to facilitate the interpretability of TKSVM we shall not average over Monte Carlo samples in which different spin planes are spontaneously selected; in fact, it suffices to analyze all samples separately. With no loss of generality, we consider a state where the ordering develops in the spin $xy$ plane, whose corresponding TKSVM pattern (coefficient matrix) is illustrated in Fig. 7. The extraction of an analytical expression for the decision function from its graphical representation is discussed in Appendix C.

The form of the decision function, Eq. (32), suggests $c_1^s$ and $c_2^s$ are independent order parameters. It follows that we can maximize $c_1^s$ and $c_2^s$ separately, and then check the consistency of their solutions. (We return to this point in Sec. VII, where $c_1^s$ and $c_2^s$ are linked explicitly to the symmetries of a tetrahedron). First, maximizing $(c_1^{xy})^2$ [i.e., solving $(c_1^{xy})^2 = 1$] leads to a manifold of spin configurations parametrized by an angle $\theta \in [0, 2\pi]$,

$$\begin{aligned}
\boldsymbol{S}_0 &= \begin{pmatrix}\cos\theta\\ \sin\theta\\ 0\end{pmatrix}, \quad \boldsymbol{S}_1 = \begin{pmatrix}\cos\theta + \frac{\pi}{2}\\ \sin\theta + \frac{\pi}{2}\\ 0\end{pmatrix},\\
\boldsymbol{S}_2 &= \begin{pmatrix}\cos\theta - \frac{\pi}{2}\\ \sin\theta - \frac{\pi}{2}\\ 0\end{pmatrix}, \quad \boldsymbol{S}_3 = \begin{pmatrix}\cos\theta + \pi\\ \sin\theta + \pi\\ 0\end{pmatrix},
\end{aligned} \tag{35}$$

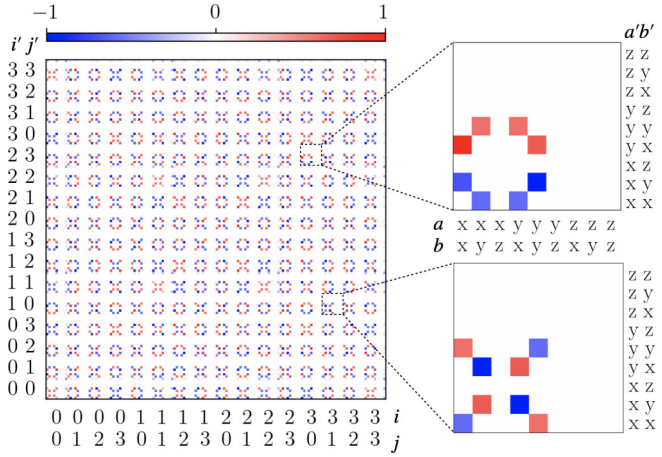



FIG. 7. Rank-2 coefficient matrix for $A$ tetrahedra. Each pixel represents the color-scaled weight of a contraction $\langle S_i^a S_j^b\rangle\langle S_{i'}^{a'} S_{j'}^{b'}\rangle$ of rank-2 features learned by the machine. The $144 \times 144$ matrix is a graphical representation of the decision function $d_A^{xy}$, with spins confined to the $xy$ plane. Long-range quadrupolar order is revealed via the magnified block patterns repeating themselves across the entire matrix. The respective weights inside these block can be interpreted as an analytical expression of the rank-2 order parameter given in Eq. (32) (see Appendix C for more details). The machine learned from spin configurations obtained by Monte Carlo simulations at $T = 4 \times 10^{-4}$ J, well below the apparent phase transition at $T_c \approx 8 \times 10^{-4}$ J in Fig. 5.

as illustrated in Fig. 8(a). Maximizing $(c_2^{xy})^2$ falls into the same structure of Eq. (35). Its evolution as a function of $\theta$ is plotted in Fig. 8(b) and shows that $(c_2^{xy})^2$ is maximized for four discrete values only:

$$\theta \in \left\{\frac{\pi}{4}, \frac{3\pi}{4}, \frac{5\pi}{4}, \frac{7\pi}{4}\right\}. \tag{36}$$

The U(1) manifold of Eq. (35) belongs to the ground state of the traditional pyrochlore antiferromagnet with negative DM interactions on *all* tetrahedra [70–72], i.e., without breathing anisotropy. Indeed, applying the spin configuration of Eq. (35) to the Hamiltonian of Eq. (1), we recover its ground-state energy per bond [70]

$$E_A^{\text{bond}} = \tfrac{1}{6}(-2J + 2\sqrt{2}D). \tag{37}$$

Since the ground-state energy of Eq. (37) is independent of $\theta$, any selection of specific $\theta$ values is necessarily due to thermal order by disorder (ObD), i.e., the selection is entropic rather than energetic.

In the standard model without breathing anisotropy, the ObD mechanism selects the $\mathbf{q} = 0$ $\Gamma_5$ long-range order [70–72]. Imposing $\theta = \frac{3\pi}{4}$ (or $\theta = \frac{7\pi}{4}$) on all tetrahedra corresponds to such a $\Gamma_5$ state, as illustrated in Fig. 8(a).

However, in our model where DM terms disappear on $B$ tetrahedra, the $B$ tetrahedra *locally* bear the ground-state degeneracy of the pyrochlore antiferromagnet. This local enhancement of the ground-state degeneracy implies that $B$ tetrahedra do not have to order into $\Gamma_5$ states anymore. As

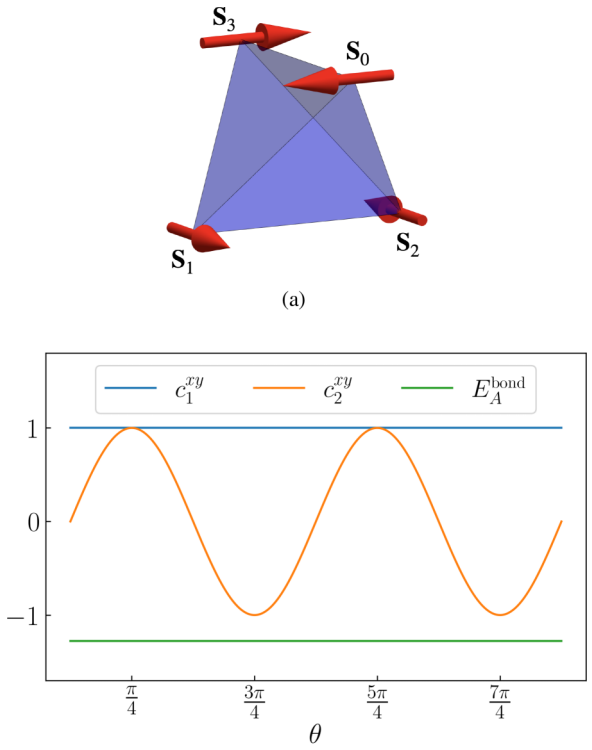



FIG. 8. Order-by-disorder in $A$ tetrahedra. (a) Example of a state maximizing both $c_1^{xy}$ and $c_2^{xy}$ with $\theta = 7\pi/4$ in Eq. (35). The bonds that lie inside the spin plane (0–3 and 1–2) have antiparallel spins. (b) The spin-plane-specific quantities $c_1^{xy}$ and $c_2^{xy}$ as well as the energy per bond, Eq. (37), with $J = 1$ and $D = -2$ as functions of the parametrization angle $\theta$. Note that in the decision function (32) the term $c_2^{xy}$ appears squared, meaning that configurations with $c_2^{xy} = -1$ are also maxima of the decision function.

a consequence, the four $A$ tetrahedra surrounding a $B$ tetrahedron are less constrained and are thus not forced to be in the same state; they have the freedom to explore different parts of the U(1) ground-state manifold of Eq. (35) independently from each other. This enhancement of the ground-state manifold is the reason why the ground state of our model of Fig. 1(b) is not simply a $\Gamma_5$ state, as confirmed by the machine which finds two additional solutions on the $A$ tetrahedra, $\theta \in \{\frac{\pi}{4}, \frac{5\pi}{4}\}$.

At this stage, the ordering mechanism is thus a two-step process. The first step is the selection of the U(1) manifold, and the second is the coalescence on special points of the manifold via thermal order by disorder. It is remarkable that the machine is able to extract both sets of solutions, by which we can infer the order-by-disorder phenomenon, out of noisy numerical data.

Now let us focus on the other type of tetrahedra, with only antiferromagnetic couplings (no DM terms). The (sub)decision function on the $B$ tetrahedra is identified as

$$d_B \sim [w_1\,(\mathbf{S}_0 \cdot \mathbf{S}_1 + \mathbf{S}_2 \cdot \mathbf{S}_3) + w_2\,(\mathbf{S}_0 \cdot \mathbf{S}_2 + \mathbf{S}_1 \cdot \mathbf{S}_3) + w_3\,(\mathbf{S}_0 \cdot \mathbf{S}_3 + \mathbf{S}_1 \cdot \mathbf{S}_2)]^2. \tag{38}$$

The values of the weights $w_1, w_2, w_3$ can be inferred from the TKSVM pattern in Fig. 9(a), satisfying

$$w_1 + w_2 + w_3 = 1, \quad \max w_i = 1, \tag{39}$$

where the maximal $w_i$ is related to the ordering spin plane in $d_A^s$. Under this constraint, $d_B$ can be intuitively maximized if the four spins in a $B$ tetrahedron are *collinear*. The solutions are listed in Table III, and Fig. 9(a) shows an example of the coefficient matrix when the ordering is in the spin $xy$ plane with $w_3 = 1$.

Alternatively, the collinearity on the $B$ tetrahedra can also be derived from the constraints on the $A$ tetrahedra derived in the previous section. Without losing generality, we again take $d_A^{xy}$ as an example. The four solutions of $(c_2^{xy})^2 = 1$ can be

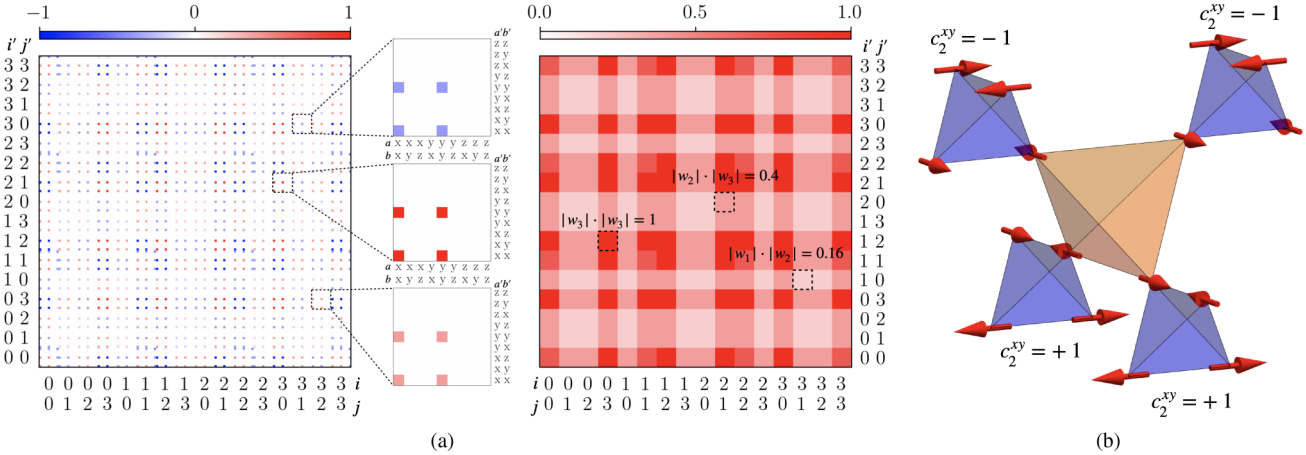



FIG. 9. (a) Rank-2 coefficient matrix for $B$ tetrahedra as a graphical representation of the decision function $d_B$. Left: Each pixel represents the color-scaled weight of a contraction $\langle S_i^a S_j^b \rangle \langle S_{i'}^{a'} S_{j'}^{b'} \rangle$ of rank-2 features learned by the machine. All blocks have the same structure but different weights. Global spin-plane selection confines all spins to the $xy$ plane. Right: Absolute weights of the coarse-grained pattern. In this specific instance, the weights of Eq. (38) are determined as $w_1 = -w_2 = 0.4$ and $w_3 = 1$. (b) Ground-state configuration with ordering in the $xy$ plane. The value of $c_2^{xy}$ is uniform within a $A$-tetrahedron layer, but alternates over different layers (cf. the upper two blue tetrahedra vs the lower two). In this example, the spin ordering plane coincides with the spatial plane.

TABLE III. Collinear ground states on $B$ tetrahedra. In each case there are two possible solutions, reflecting the $\mathbb{Z}_2$ symmetry. The leftmost column describes which spatial layer possesses the $\mathbb{Z}_2$ symmetry, while the rightmost column indicates which of the three possible configurations of the $B$ tetrahedra, defined in Eq. (50), is not allowed.

| Spatial layer | Maximal weight | $(\boldsymbol{S}_0 \cdot \boldsymbol{S}_1)$ | $(\boldsymbol{S}_0 \cdot \boldsymbol{S}_2)$ | $(\boldsymbol{S}_0 \cdot \boldsymbol{S}_3)$ | $(\boldsymbol{S}_1 \cdot \boldsymbol{S}_2)$ | $(\boldsymbol{S}_1 \cdot \boldsymbol{S}_3)$ | $(\boldsymbol{S}_2 \cdot \boldsymbol{S}_3)$ | Missing config. |
|---|---|---|---|---|---|---|---|---|
| $yz$ | $w_1 = 1$ | $-1$ | $\pm 1$ | $\mp 1$ | $\mp 1$ | $\pm 1$ | $-1$ | $P(\boldsymbol{\Lambda}_E^{\star 1}) = 0$ |
| $xz$ | $w_2 = 1$ | $\pm 1$ | $-1$ | $\mp 1$ | $\mp 1$ | $-1$ | $\pm 1$ | $P(\boldsymbol{\Lambda}_E^{\star 2}) = 0$ |
| $xy$ | $w_3 = 1$ | $\pm 1$ | $\mp 1$ | $-1$ | $-1$ | $\mp 1$ | $\pm 1$ | $P(\boldsymbol{\Lambda}_E^{\star 3}) = 0$ |

divided into two classes

$$c_2^{xy} = 1: \quad \boldsymbol{S}_0 = \frac{1}{\sqrt{2}}\begin{pmatrix}1\\1\\0\end{pmatrix}, \quad \boldsymbol{S}_1 = \frac{1}{\sqrt{2}}\begin{pmatrix}-1\\1\\0\end{pmatrix},$$
$$\boldsymbol{S}_2 = \frac{1}{\sqrt{2}}\begin{pmatrix}1\\-1\\0\end{pmatrix}, \quad \boldsymbol{S}_3 = \frac{1}{\sqrt{2}}\begin{pmatrix}-1\\-1\\0\end{pmatrix}, \tag{40}$$

$$c_2^{xy} = -1: \quad \boldsymbol{S}_0 = \frac{1}{\sqrt{2}}\begin{pmatrix}1\\-1\\0\end{pmatrix}, \quad \boldsymbol{S}_1 = \frac{1}{\sqrt{2}}\begin{pmatrix}1\\1\\0\end{pmatrix},$$
$$\boldsymbol{S}_2 = \frac{1}{\sqrt{2}}\begin{pmatrix}-1\\-1\\0\end{pmatrix}, \quad \boldsymbol{S}_3 = \frac{1}{\sqrt{2}}\begin{pmatrix}-1\\1\\0\end{pmatrix}, \tag{41}$$

up to a global sign flip which preserves the value of $c_2^{xy}$. Equations (40) and (41) correspond to $\theta \in \{\frac{\pi}{4}, \frac{5\pi}{4}\}$ and $\{\frac{3\pi}{4}, \frac{7\pi}{4}\}$, respectively. Measurements of this machine-learned quantity show that $c_2^{xy} = \pm 1$ *alternates* through the $z$ direction, as shown in Fig. 9(b). As a $B$ tetrahedron shares spins with four $A$ tetrahedra, it has to take two collinear spins from Eq. (40) and then two spins with the same collinearity from Eq. (41). Otherwise, it cannot satisfy the staggered distribution $c_2^{xy} = \pm 1$. This long-range order breaks spin-rotation, spin-permutation, and translational symmetry.

## V. SIMULATIONS AFTER AI INPUT

Equipped with the new insights on the structure of the ground state, we return to Monte Carlo simulations. This time instead of slowly annealing from high temperature, we initialize the system by quenching into the configuration of Fig. 1(b) at temperature $T$, followed by $10^6$ MC steps of thermalization, and $10^7$ MC steps for measurements. Paving the lattice with the ground state found by the machine requires alternating along the $z$ direction, the $xy$ layers of spin configurations as in Fig. 9(b) with their time-reversal symmetric. This naturally forms a 32-site magnetic unit cell [see Fig. 1(b)]. We have again 126 temperatures equally spaced between 0 and 0.0025 J, and use heat-bath, parallel-tempering, and overrelaxation algorithms. The results are shown in Fig. 10, computed for the same physical parameters mentioned in Sec. III.

These new MC simulations converge nicely and confirm the stability of the ground state found by the machine. The transition is now violently first order, whose hysteresis explains the shift of the transition temperature $T_c$ between $0.8\,10^{-3}$ J in Fig. 5 and $1.5 \times 10^{-3}$ J in Fig. 10. Quenched simulations in the latter case provide an upper bound of $T_c$, while slow annealing has more difficulty in finding the ordered phase and provides a lower bound to $T_c$. The $c_1$ and $c_2$ order parameters correctly describe the ground state, with a noticeably stronger finite-size dependence for the latter: a common consequence of the order-by-disorder mechanism [84]. Finally, the order parameter $m_{q=W}$ now saturates

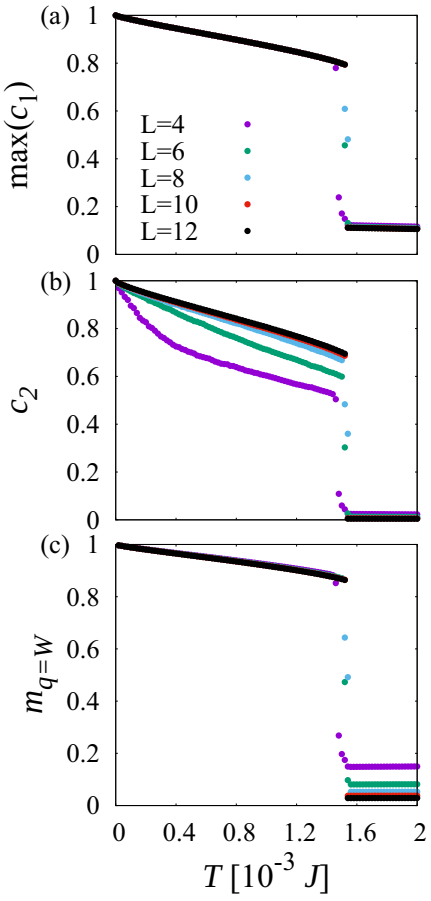



FIG. 10. Classical Monte Carlo (MC) simulation results for breathing pyrochlore model after input from machine learning, showing good equilibration in the ordered phase for $T \lesssim 1.5 \times 10^{-3}$ J. (a) Rank-1 order parameter $c_1$, corresponding to dipolar order. (b) Rank-2 order parameter $c_2$, corresponding to quadrupolar order. (c) Staggered magnetization $m_{\mathbf{q}}$ at wave vector $\mathbf{q} = W$. Simulations were carried out for the model (1), for a clusters with linear dimension $L \in \{4, 6, 8, 10, 12\}$, with parameters (31). Further details, including the definitions of the order parameters $c_1$ and $c_2$, can be found in Sec. V.

at $T = 0$, which means there is *a priori* no coexistence of other phases.

## VI. EMERGENT $\mathbb{Z}_2$ PLANAR SYMMETRY

We now put the machine-learned quantities together and discuss an emergent planar-flip symmetry, which will also resolve the origin of the irregular weights in Fig. 6. For simplicity, we continue to consider the ground state of Fig. 1(b) as an example, where the order is developed in the $xy$ plane and the planar symmetry acts on spatial $xy$ planes. In general these two planes do not need to coincide, but this does not affect our discussion: the spin-order plane is manifest from the $c_1$ and $c_2$ parameters, while the direction of the spatial planar-flip symmetry can be known from the largest weight in $d_B$.

Given the collinearity on the $B$ tetrahedron, the decision function (38) reduces to

$$d_B \sim (-w_1 - w_2 + w_3)^2 = (w_3)^2. \tag{42}$$

Here we have used the solutions in Eqs. (40) and (41) (or equivalently the corresponding configuration in Table III) and the weight relation in Eq. (39). As in this example $\max w_i = w_3 = 1$, the relation Eq. (39) reduces to $w_1 + w_2 = 0$.

Equation (42) manifests a property of $d_B$ that it is invariant under flipping a specific pair of spins, which can be $(\mathbf{S}_0, \mathbf{S}_3)$ or $(\mathbf{S}_1, \mathbf{S}_2)$ in the current example. Nevertheless, as spins in a $B$ tetrahedron belong to different $A$ tetrahedra, in order to preserve the value of the order parameters $c_1$ and $c_2$, one has to flip all spins in the two neighboring $A$ tetrahedra. This procedure is then repeated to further $A$-tetrahedra neighbors, and closes only after flipping the spins in an entire layer $dA$ of $A$-sublattice tetrahedra

$$\mathbf{S}_i \to -\mathbf{S}_i \quad \forall \quad i \in dA \tag{43}$$

as illustrated in Fig. 11.

Namely, there is an *emergent* subsystem symmetry acting on individual ordering layers of $A$ tetrahedra (equivalently, two adjacent $B$-tetrahedron layers, while only the bottom or top half of each $B$ layer is transformed). As a consequence, the system "hybridizes" rank-1 and rank-2 orders. This is a rather unconventional emergent property for an ordered phase; such subextensive zero modes usually require to be artificially enforced via either a global or local symmetry of the system [82,85,86].

Since this planar spin flip is subextensive (the number of spins involved scales as $L^2$) we expect it to be dynamically robust. Pragmatically, let us assume that while cooling down the system, such a planar spin flip takes place. This is quite possible since it costs zero energy and the transition is violently first order (see Fig. 10); once the cubic symmetry is broken in favor of a given plane (here the $xy$ plane), two far-away layers of $A$ tetrahedra may likely order independently from each other. As a result, the long-range dipolar order with Bragg peaks at $\mathbf{q} = W$ found in Fig. 10 will be perturbed by multiple planar spin flips at random positions in the system. And since there is a vanishingly small probability to move $L^2$ spins coherently in the thermodynamic limit, such energetically degenerate spin configuration should remain stable over very long timescales.

This mechanism explains the origin of the irregular weights in Fig. 6, and probably played an important role in the difficulty to interpret previous Monte Carlo simulations, by hindering the ordering mechanism and hiding the magnetic dipolar order. As a result, the magnetic order will only be long range within the plane. The interplane ordering is quadrupolar and defined by $c_1$ and $c_2$ in Eqs. (33) and (34), akin to spin nematics [87] but only in the spatial direction orthogonal to the magnetic layers. Moreover, the translational symmetry is preserved along this orthogonal direction, while the lattice rotation symmetry is spontaneously broken due to the emergent planar spin flips. This is reminiscent of the smectic phase in liquid crystal physics, which breaks spatial rotational symmetry but only partially breaks translational symmetries [88]. Therefore, in addition to the in-plane magnetic orders, such states share interesting features of both spin nematics (quadrupolar order) and smectics (layered structure).

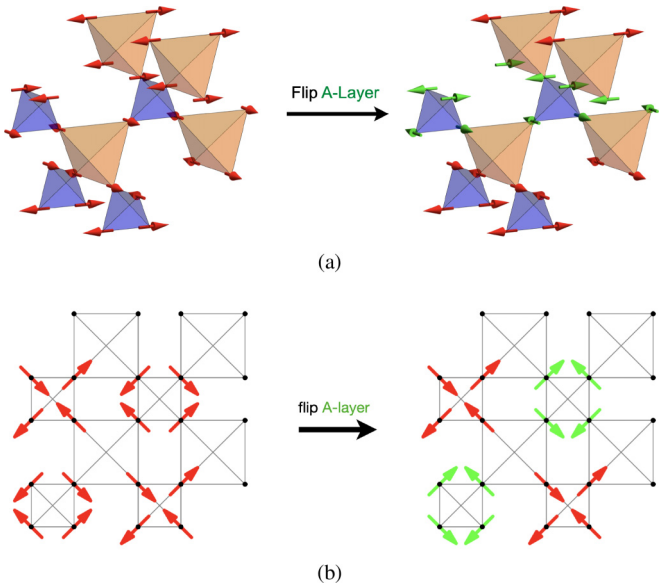



FIG. 11. Visual representation of planar $\mathbb{Z}_2$ symmetry. (a) All $A$ tetrahedra within one layer are flipped, following Eq. (43), thereby changing the value of $\mathbf{\Lambda}_E$ [Eq. (45)] in the two neighboring $B$ layers. On $B$ tetrahedra, only intralayer bonds connecting two $A$ tetrahedra from the same layer are affected by the transformation. (b) Equivalent transformation, viewed in a projection onto the $xy$ plane; for simplicity, not all spins are drawn. This example shows a case where the normal on the spin plane coincides with the normal on the layer partitioning, but in general we can also construct ground states where the two normals do not coincide. In all cases, the spins changed by the $\mathbb{Z}_2$ transformation are indicated in green.

To conclude, we should mention that among all of the energetically degenerate states connected by $\mathbb{Z}_2$ symmetry, three of them have the 16-site cubic unit cell of Fig. 9(b) paving the entire lattice. They possess two planar symmetries rather than only one, e.g., planar $xy$ and $yz$ symmetries with the corresponding weights $w_1 = w_3 = 1, w_2 = -1$ (cf. Table III). But any planar spin flip as in Fig. 11 would immediately break the fragile cubic symmetry.

## VII. RELATIONSHIP IRREPS OF $T_d$

TKSVM learns order parameters in the language of the raw data, namely, the ordinary spin degrees of freedom. To

gain more insight, we can cast the machine-learned quantities in terms of the irreducible representations of the point group $T_d$ [84], which reflect the human way of thinking about the problem.

Following the definitions given in Sec. II D, the two order parameters found in the decision function in $d_A^s$ can be expressed in terms of irreps of $T_d$ as

$$c_1^s = \tfrac{1}{4}\left(\left\|\boldsymbol{m}_{T_{1-}}\right\|^2 + \left\|\boldsymbol{m}_E\right\|^2\right), \tag{44a}$$

$$c_2^s = \tfrac{1}{4}\left(\left\|\boldsymbol{m}_{T_{1-}}\right\|^2 - \left\|\boldsymbol{m}_E\right\|^2\right). \tag{44b}$$

We see that $c_1^s$ reproduces the ground-state constraint of the rank-2 U(1) gauge theory, but with an additional index $s \in \{xy, xz, yz\}$ for the spontaneous selection of a spin plane. The order parameter $c_2^s$ is nevertheless an emergent quantity that is not evident from direct symmetry arguments. The meaning of the ground-state condition $c_2^s = \pm 1$ now becomes more intuitive in this irrep basis. Order by disorder selects states on $A$-sublattice tetrahedra which transform with either $\boldsymbol{m}_{T_{1-}}$ or $\boldsymbol{m}_E$. The alteration of $c_2^s = \pm 1$ further means that the system can be viewed as staggered layers of $\boldsymbol{m}_{T_{1-}}$ and $\boldsymbol{m}_E$ $A$ tetrahedra.

For the $B$-sublattice tetrahedra, it is more convenient to work with bond-based irreps discussed in [89]

$$\begin{pmatrix} \Lambda_{A_1} \\ \Lambda_{E,1} \\ \Lambda_{E,2} \\ \Lambda_{T_2,1} \\ \Lambda_{T_2,2} \\ \Lambda_{T_2,3} \end{pmatrix} = \begin{pmatrix} \frac{1}{\sqrt{6}} & \frac{1}{\sqrt{6}} & \frac{1}{\sqrt{6}} & \frac{1}{\sqrt{6}} & \frac{1}{\sqrt{6}} & \frac{1}{\sqrt{6}} \\ \frac{1}{\sqrt{3}} & -\frac{1}{2\sqrt{3}} & -\frac{1}{2\sqrt{3}} & -\frac{1}{2\sqrt{3}} & -\frac{1}{2\sqrt{3}} & \frac{1}{\sqrt{3}} \\ 0 & \frac{1}{2} & -\frac{1}{2} & -\frac{1}{2} & \frac{1}{2} & 0 \\ 0 & 0 & -\frac{1}{\sqrt{2}} & \frac{1}{\sqrt{2}} & 0 & 0 \\ 0 & -\frac{1}{\sqrt{2}} & 0 & 0 & \frac{1}{\sqrt{2}} & 0 \\ -\frac{1}{\sqrt{2}} & 0 & 0 & 0 & 0 & \frac{1}{\sqrt{2}} \end{pmatrix} \begin{pmatrix} \boldsymbol{S}_0 \cdot \boldsymbol{S}_1 \\ \boldsymbol{S}_0 \cdot \boldsymbol{S}_2 \\ \boldsymbol{S}_0 \cdot \boldsymbol{S}_3 \\ \boldsymbol{S}_1 \cdot \boldsymbol{S}_2 \\ \boldsymbol{S}_1 \cdot \boldsymbol{S}_3 \\ \boldsymbol{S}_2 \cdot \boldsymbol{S}_3 \end{pmatrix}, \tag{45}$$

where the convention for numbering sites is defined in Appendix A. Once transcribed in this basis, the decision function $d_B$ becomes

$$d_B \sim \left[a_{A_1}\Lambda_{A_1} + a_{E,1}\Lambda_{E,1} + a_{E,2}\Lambda_{E,2}\right]^2, \tag{46}$$

with coefficients

$$a_{A_1} = \sqrt{\frac{2}{3}}\,(w_1 + w_2 + w_3), \tag{47}$$

$$a_{E,1} = \sqrt{\frac{1}{3}}\,(2w_1 - w_2 - w_3), \tag{48}$$

$$a_{E,2} = w_2 - w_3. \tag{49}$$

Maximizing $d_B$, subject to the constraint of fixed spin length, requires $\Lambda_{A_1} \equiv -\sqrt{\frac{2}{3}}$ and that $\boldsymbol{\Lambda}_E$ take on one of three possible representations

$$\boldsymbol{\Lambda}_E^{\star 1} = \begin{pmatrix} \frac{4}{\sqrt{3}} \\ 0 \end{pmatrix}, \quad \boldsymbol{\Lambda}_E^{\star 2} = \begin{pmatrix} \frac{-2}{\sqrt{3}} \\ 2 \end{pmatrix}, \quad \boldsymbol{\Lambda}_E^{\star 3} = \begin{pmatrix} \frac{-2}{\sqrt{3}} \\ -2 \end{pmatrix}, \tag{50}$$

which are the three maxima of $\|\boldsymbol{\Lambda}_E\|^2$ under the condition of minimal $\Lambda_{A_1}$.

These three configurations are transformed by the $\mathbb{Z}_2$ planar symmetry, as depicted in Fig. 12. Nevertheless, we can infer the distribution of $\boldsymbol{\Lambda}_E$, $\{P(\boldsymbol{\Lambda}_E^{\star 1}), P(\boldsymbol{\Lambda}_E^{\star 2}), P(\boldsymbol{\Lambda}_E^{\star 3})\}$, over all the $B$ tetrahedra from the weights of $d_B$ in Eq. (38). Specifically, we denote $\boldsymbol{a}_E^{\star 1}, \boldsymbol{a}_E^{\star 2}, \boldsymbol{a}_E^{\star 3}$ to be the respective coefficients in the extreme cases where all $B$ tetrahedra are in the same $\boldsymbol{\Lambda}_E$ configuration,

$$\boldsymbol{a}_E^{\star 1} = \begin{pmatrix} \frac{-4}{\sqrt{3}} \\ 0 \end{pmatrix}, \quad \boldsymbol{a}_E^{\star 2} = \begin{pmatrix} \frac{2}{\sqrt{3}} \\ -2 \end{pmatrix}, \quad \text{or} \quad \boldsymbol{a}_E^{\star 3} = \begin{pmatrix} \frac{2}{\sqrt{3}} \\ 2 \end{pmatrix}. \tag{51}$$

In addition, $a_{A_1} = \sqrt{2/3}$ reflects the ground-state condition $\Lambda_{A_1} = -\sqrt{2/3}$ which is independent of $\boldsymbol{\Lambda}_E$. The general coefficients $a_{A_1}, a_{E,1}, a_{E,2}$ are then solved from a set of linear equations

$$\begin{pmatrix} a_{A_1} & a_{A_1} & a_{A_1} \\ a_{E,1}^{\star 1} & a_{E,1}^{\star 2} & a_{E,1}^{\star 3} \\ a_{E,2}^{\star 1} & a_{E,2}^{\star 2} & a_{E,2}^{\star 3} \end{pmatrix} \begin{pmatrix} P(\boldsymbol{\Lambda}_E^{\star 1}) \\ P(\boldsymbol{\Lambda}_E^{\star 2}) \\ P(\boldsymbol{\Lambda}_E^{\star 3}) \end{pmatrix} = \begin{pmatrix} a_{A_1} \\ a_{E,1} \\ a_{E,2} \end{pmatrix}. \tag{52}$$

Here the first equation reduces to the normalization of the distribution $\sum_i P(\boldsymbol{\Lambda}_E^{\star i}) = 1$, equivalent to $\sum_i w_i = 1$. In the example of Fig. 9(a), the weights are given by $w_1 = -w_2 = 0.4$ and $w_3 = 1$ which translates to $a_{A_1} = \sqrt{2/3}$, $a_{E,1} = \sqrt{1/3} \times 0.2$ and $a_{E,2} = -1.4$. Solving the linear system for these values yields

$$P(\boldsymbol{\Lambda}_E^{\star 1}) = 0.3, \quad P(\boldsymbol{\Lambda}_E^{\star 2}) = 0.7, \quad P(\boldsymbol{\Lambda}_E^{\star 3}) = 0. \tag{53}$$

In general there is always one vanishing $P(\boldsymbol{\Lambda}_E^{\star i})$, which is equivalent to have maximal weight $\max w_i = 1$ and can be associated with the spatial orientation of the planar $\mathbb{Z}_2$ symmetry, as listed in Table III.

From this analysis is clear that the decision function constructed by the SVM in its attempt to classify data for the unknown ordered phase has a natural interpretation in terms of physical quantities, namely, the symmetries of a tetrahedron within the pyrochlore lattice. In a simpler problem, the irrep corresponding to the ordered state might have been deduced, or even intuited, by a human researcher. However, in the present case, many different irreps are involved, and even the form of irrep needed changes from $A$- to $B$-sublattice tetrahedra. At this level of complexity, it would be very hard for a human researcher to arrive at the combination of irreps required to classify the unknown order without the guiding hand of the machine.

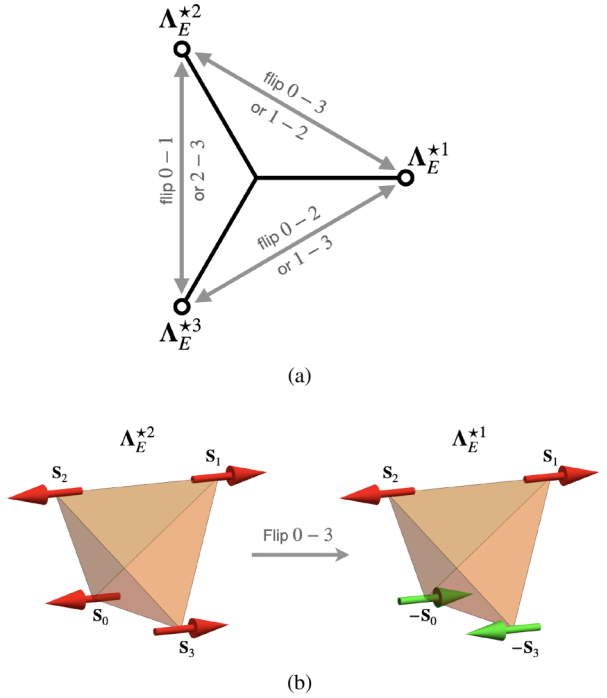



FIG. 12. Bond-based irreps of the tetrahedral symmetry group $T_d$ appearing in the decision function found in analysis of the phase with undetermined order. (a) Relationship between representations which maximize $\|\mathbf{\Lambda}_E\|^2$ [Eq. (50)] under $\mathbb{Z}_2$ bond-flip operations [Eq. (43)]. (b) Illustration of action of $\mathbb{Z}_2$ bond-flip operation on a specific pair of representations, showing how one configuration maximizing $\|\mathbf{\Lambda}_E\|^2$ is mapped onto another. Bonds with antiparallel spins are highlighted in green.

## VIII. SUMMARY AND CONCLUSIONS

Although artificial intelligence (AI) brings the opportunity to automate many of the routine, repeated, tasks which arise in scientific research, it remains an open question how far AI will impact on the creative, conceptual, and problem-solving aspects of science. Here, we have shown how researchers trying to understand a difficult problem in frustrated magnetism, and faced with poorly thermalized Monte Carlo simulations, benefit from working with AI.

The problem considered was the form of low-temperature order achieved in a model of breathing pyrochlore magnets [Eq. (1)], as the result of a phase transition out of classical spin liquid described by a higher-rank gauge theory (cf. Sec. II A). Earlier Monte Carlo (MC) simulations (Yan *et al.*, Ref. [53]), were successful in characterizing the spin liquid, and identified a phase transition into an ordered state at very low temperature. However, simulation results at the lowest temperatures were too poorly thermalized for the form of order to be identified by conventional means (cf. Sec. III).

In this article, we have demonstrated how a highly interpretable form of machine learning, the support vector machine with tensorial kernel (TKSVM), can be used to reanalyze the same noisy MC data, gaining critical insights into the underlying correlations, without the need for prior training or supervision. By using kernels based on both rank-1 and rank-2 tensors, we obtain information about both dipolar and quadrupolar correlations within spin configurations at low temperatures.

Considering first the rank-1 tensor (Sec. IV A), we found that MC results are inconsistent with conventional magnetic order, confirming that a more complex mechanism is at work. Turning to the rank-2 tensor (Sec. IV B), we learn that there are three global spin planes, $xy$, $xz$, and $yz$, which spontaneously break the spin rotation symmetry on the $A$-sublattice tetrahedra. These correlations are captured by a local order parameter $c_1$ [Eq. (33)], which selects a (sub)manifold of the degenerate states contributing to the spin liquid, characterized by an emergent U(1) degree of freedom [Eq. (35)]. A second local order parameter $c_2$ [Eq. (34)] further selects four discrete states from this U(1) manifold [Eq. (36)].

Applying TKSVM to $B$-sublattice tetrahedra then brings forward the full three-dimensional magnetic structure, i.e., how these four discrete states pave the entire lattice together.

We then returned to MC simulation, armed with what had been learned through the application of machine learning (Sec. V). By generating spin configurations that satisfy the constraints imposed by the local order parameters $c_1$ and $c_2$, we are able to initialize MC simulations within the manifold of states favored at low temperatures. Doing so, we found that simulations converge nicely (Fig. 10), confirming the validity of the machine-learning analysis, and leading to a consistent estimate of the ordering temperature.

As well as facilitating improved simulations, machine-learning results also teach us about the deeper structure of the manifold of states favored at low temperatures. In Sec. VI we revisited the decision function found by the TKSVM, and show how it is invariant under operations which "flip" all spins within an entire layer of $A$-sublattice tetrahedra. From this we infer the existence of an emergent $\mathbb{Z}_2$ symmetry, associated with planes of tetrahedra. This leads to a picture which has much in common with a smectic liquid crystal, in which translational symmetries are (partially) broken by parallel planes of molecules that align to common axis.

Finally, we considered how machine-learning results might be interpreted in terms of a more conventional language of symmetry operations (Sec. VII). We found that the local order parameter $c_1$ could be expressed in terms of the irreps of the symmetry group of a tetrahedron $T_d$ (Appendix A). Comparing this with the theory of the spin liquid found at higher temperature [53], we learned that the low-temperature order satisfies the emergent Gauss' law which defines the spin liquid, and can be associated with fluctuation of the electric field tensor of the associated higher-rank gauge theory.

These results are remarkable in a number of ways. First, they demonstrate the power of the machine-learning approach in extracting meaningful physical information from noisy MC data. Despite the fact that low-temperature simulations were of too poor quality to be interpreted by human researchers, the decision function extracted from TKSVM analysis contains sufficient information to reconstruct fluctuations of a rank-2 electric field. This is even more surprising, given that the result was obtained without any prior training or supervision: at no point was the AI "taught" about existence of a tensor electric field within the parent spin-liquid phase, let alone its possible role in low-temperature order.

In rediscovering a key organizational principle, and pinpointing how this relates to an unidentified form of low-temperature order, the AI is performing a role which would usually be associated with the creative thinking of a human researcher. But this is not to say that AI entirely replaced, or superceded, human insight. Instead, the analysis of the decision function found through the TKSVM provided the "missing link" needed for a team of human researchers to resolve the remaining open questions.

In this respect, the input from AI played exactly the same role as the input from any human researcher who provides a critical insight into an unsolved problem. Ultimately, the solution was accomplished by combining the input from AI with human insights into breathing pyrochlore model, and through new MC simulations seeded from spin configurations generated using the help of the TKSVM. This interplay of ideas generated by humans, and ideas (or more precisely, equations) generated by a machine, follows the familiar pattern of collaboration within a team of researchers, each of whom makes their own, interdependent, contribution to the solution of a problem.

Within the field of frustrated magnetism, there any many other problems which might benefit from such an approach. In our case, it was crucial to have a very strongly interpretable algorithm, but analytical and group-theoretical arguments were also indispensable. We do not expect all noisy simulations to be tractable this way. For instance, the critical slowing down witnessed in second-order phase transitions would be especially challenging since it requires updates acting at different length scales. That being said, our approach is sufficiently general that it can be applied to a variety of complex unknown phases. What immediately comes to mind are other frustrated magnets such as the Gd pyrochlores [90,91] and Mn-kagome [92] with multi-$k$ orders, the subtle ordering of dipolar pyrochlores [93,94], or Kitaev magnets [95–97]. As the TKSVM algorithm has also been extended to quantum problems [98], our strategy is not confined to classical physics, and could even be combined with the field of quantum simulation.

More generally, the "collaborative" nature of the interactions between human researchers and machines described in this paper becomes possible wherever the output of machine learning can be translated into a form which can be understood and manipulated by humans, such as the equations implied by the decision function of a support vector machine. While the TKSVM is ideally suited to such an approach, it is not the only interpretable form of machine learning, and even approaches that are not directly interpretable, such as deep neural networks, may provide critical insights into unsolved problems. As such this model of collaboration offers one possible paradigm for AI-driven research in an age in which human and machine have complementary strengths.

## ACKNOWLEDGMENTS

N.S., K.L., and L.P. acknowledge support from FP7/ERC Consolidator Grant QSIMCORR, No. 771891, and the Deutsche Forschungsgemeinschaft (DFG, German Research Foundation) under Germany's Excellence Strategy, Grant No. EXC-2111 - 390814868. L.D.C.J. acknowledges financial support from CNRS (PICS France-Japan MEFLS) and from the French "Agence Nationale de la Recherche" under Grants No. ANR-18-CE30-0011-01 and No. ANR-23-CE30-0038-01. K.L. acknowledges support from the New Cornerstone Science Foundation through the XPLORER PRIZE, Anhui Initiative in Quantum Information Technologies, and Shanghai Municipal Science and Technology Major Project (Grant No. 2019SHZDZX01). N.S. acknowledges financial support from the Theory of Quantum Matter Unit, OIST, and JSPS KAKENHI Grants No. JP19H05822 and No. JP19H05825.

## APPENDIX A: DEFINITIONS AND CONVENTIONS

In this Appendix we provide lattice and model definitions, and our conventions for the order parameters of the irreps of the $T_d$ group. The sites of an $A$ tetrahedron are located at

$$\boldsymbol{r}_0 = \frac{a}{8}(1,1,1), \quad \boldsymbol{r}_1 = \frac{a}{8}(1,-1,-1),$$
$$\boldsymbol{r}_2 = \frac{a}{8}(-1,1,-1), \quad \boldsymbol{r}_3 = \frac{a}{8}(-1,-1,1)$$

relative to the center of an $A$ tetrahedron, as in [99]. Here, $a$ is the length of the fcc unit cell. The sites of a $B$ tetrahedron are located at $-\boldsymbol{r}_0, -\boldsymbol{r}_1, -\boldsymbol{r}_2, -\boldsymbol{r}_3$ relative to the center of a $B$ tetrahedron.

The bond-dependent DM-interaction vectors are defined as [70,100]

$$\boldsymbol{d}_{01} = \frac{(0,-1,1)}{\sqrt{2}}, \quad \boldsymbol{d}_{02} = \frac{(1,0,-1)}{\sqrt{2}}, \quad \boldsymbol{d}_{03} = \frac{(-1,1,0)}{\sqrt{2}},$$
$$\boldsymbol{d}_{12} = \frac{(-1,-1,0)}{\sqrt{2}}, \quad \boldsymbol{d}_{13} = \frac{(1,0,1)}{\sqrt{2}}, \quad \boldsymbol{d}_{23} = \frac{(0,-1,-1)}{\sqrt{2}}.$$

We do not consider models with DM couplings $D_B$ on $B$ tetrahedra because $D_B$ lifts the degeneracy of the rank-2 spin liquid, thus stepping away from our motivation to study the ordering mechanism within a higher-rank gauge theory. Nevertheless, even if it can be expected to be much smaller than on $A$ tetrahedra $D_B \ll D_A$, $D_B$ is allowed by symmetry. If $D_B < 0$, then the system should ultimately order the same way as for nonbreathing pyrochlores, i.e., via order by disorder within $\Gamma_5$ states [70–72]. If $D_B > 0$, there would be an energetic competition between $\Gamma_5$ and all-in–all-out states depending on the ratio $D_A/D_B$. Note that if $0 < |D_B| \ll T_c$ then we should recover the physics discussed in this paper at $T_c$ before a second phase transition at lower temperatures.

## APPENDIX B: TKSVM

This Appendix aims at providing the reader with the essential working principles of the tensorial-kernel support vector machine (TKSVM). The TKSVM approach is an interpretable and (quasi)unsupervised machine-learning algorithm developed in Refs. [23,26,24] and recently also extended to quantum problems [98].

Considering classical $O(3)$-spin configurations (i.e., Monte Carlo snapshots) $\mathbf{x} = \{S_i^a | i = 1, 2, \ldots, N; a = x, y, z\}$, the first step of TKSVM is the construction of feature vectors

$\boldsymbol{\phi} = \{\phi_\mu\}$ consisting of degree-$n$ monomials from $\mathbf{x}$,

$$\phi_\mu = \left\langle S_{\alpha_1}^{a_1} S_{\alpha_2}^{a_2} \dots S_{\alpha_n}^{a_n} \right\rangle_{\mathrm{cl}}, \tag{B1}$$

where $\langle \dots \rangle_{\mathrm{cl}}$ represents a lattice average over predetermined nonoverlapping clusters, each containing $r$ spins, where $\alpha_1, \dots, \alpha_n$ label spins within the cluster, and where $\mu = \{\alpha_1, a_1; \dots; \alpha_n, a_n\}$ denotes a composite index. The tensorial feature space spanned by $\{\phi_\mu\}$ hosts any potential classical spin order of degree $n$ that fits within the predefined cluster of size $r$. Following the construction of feature vectors from the input data, TKSVM detects the underlying order during the learning stage, provided that the user made a suitable choice of the hyperparameters $n$ and $r$. The optimal choice of $n$ and $r$ are unknown *a priori*. Therefore, we choose clusters in accordance with the unit cell of the lattice and Hamiltonian interactions, and increase $n$ systematically on a trial-and-error basis until TKSVM succeeds. In this approach $n = 1$ allows the detection of magnetic orders, and higher $n > 1$ detects multipolar orders and emergent local constraints.

A central concept of SVM methods is the decision function $d$. The decision function can be written as a product $d = \mathbf{V}^t \hat{\mathbf{C}} \mathbf{V}$ up to a constant known as the bias. Here, $\mathbf{V}$ is a vector made of input data and $\hat{\mathbf{C}} = \{C_{\mu\nu}\}$ is the output of the machine in the form of a coefficient matrix measuring correlations of $\phi_\mu$,

$$C_{\mu\nu} = \sum_k \lambda_k \phi_\mu(\mathbf{x}^{(k)}) \phi_\nu(\mathbf{x}^{(k)}), \tag{B2}$$

where the Lagrange multiplier $\lambda_k$ denotes the weight of the $k$th sample. The nonvanishing entries of $C_{\mu\nu}$ identify the relevant basis tensors of the tensorial feature space, and their interpretation yields analytical expressions of the underlying order parameters. As TKSVM has never learned nor seen any of the different phases, it has the advantage of being unbiased in identifying them. Compared to a human approach where one would define an order parameter and then test it on the Monte Carlo data, the approach in TKSVM is blind to specifying order-parameter candidates and looks for all possibilities within the search space spanned by the rank-$r$ monomials defined on the cluster of size $n$.

## APPENDIX C: PATTERN INTERPRETATION

The last step of TKSVM consists of constructing the analytical expression of the underlying order from the internal parameters of the learning model. This is achieved by reading off and interpreting the graphical representation (pattern) of the coefficient matrix. Since the underlying order in this case is fairly complex, we shall discuss the procedure for a subset of the full pattern for the $A$ tetrahedra only. Specifically, we start by considering the block with spin indices (2 3, 3 0); see the upper zoomed-in panel of Fig. 7.

Reading off the terms from the block pattern with coefficients approximated as $\pm 1$ yields the expression

$$\begin{aligned}[d_A]_{(2\,3,3\,0)} \sim\ & +\left(S_2^y S_3^x\right)\left(S_3^x S_0^x\right) + \left(S_2^y S_3^x\right)\left(S_3^y S_0^y\right) - \left(S_2^x S_3^y\right)\left(S_3^x S_0^x\right) \\ & - \left(S_2^x S_3^y\right)\left(S_3^y S_0^y\right) + \left(S_2^y S_3^y\right)\left(S_3^x S_0^y\right) + \left(S_2^y S_3^y\right)\left(S_3^y S_0^x\right) \\ & - \left(S_2^x S_3^x\right)\left(S_3^y S_0^y\right) - \left(S_2^x S_3^x\right)\left(S_3^y S_0^x\right).\end{aligned} \tag{C1}$$

In order to reshape the expression into a sum over square magnitudes of rank-2 order parameters, we factorize the feature components and assign the coefficients (signs) in consistency with other block patterns (2 3, 2 3), (3 0, 3 0), and (3 0, 2 3):

$$\begin{aligned}&[d_A]_{(2\,3,3\,0)} + [d_A]_{(3\,0,2\,3)} + [d_A]_{(2\,3,2\,3)} + [d_A]_{(3\,0,3\,0)} \\ &\quad \sim \left(-S_2^y S_3^x + S_2^x S_3^y - S_3^x S_0^x - S_3^y S_0^y\right)^2 \\ &\qquad + \left(+S_2^x S_3^x - S_2^y S_3^y - S_3^x S_0^y - S_3^y S_0^x\right)^2.\end{aligned} \tag{C2}$$

We factorize even further, which requires to consider some more block patterns

$$\begin{aligned}\sum_{ij,i'j' \in \{0,2,3\}} [d_A]_{(i\,j,i'\,j')} \sim\ & -\left[S_0^x - S_2^y - S_3^x\right)^2 + \left(S_0^y + S_2^x - S_3^y\right)^2\Big]^2 \\ & - \left[2\left(S_0^x - S_2^y - S_3^x\right)\left(S_0^y + S_2^x - S_3^y\right)\right]^2.\end{aligned} \tag{C3}$$

This expression already contains a substantial part of the full decision function. Comparing to the definition of $c_1^{xy}$ and $c_2^{xy}$ in Eqs. (33) and (34), respectively, reveals that only the terms including $\mathbf{S}_1$ are missing.

Extending the interpretation to the full pattern, we arrive at the expression

$$d_A = \sum_{\substack{ij,i'j' \\ \in\{0,1,2,3\}}} [d_A]_{(i\,j,i'\,j')} \sim -\left[\left(c_1^{xy}\right)^2 + \left(c_2^{xy}\right)^2\right]. \tag{C4}$$

Note that the overall minus sign is of technical origin and is arbitrary in each TKSVM run, hence it can be dropped. The sign convention in Eq. (32) is chosen to match with the signs in the existing definition of $\mathbf{m}_{T_{1-}}$ (see its third component in Table I for comparison). Furthermore a factor of $\frac{1}{16}$ was introduced to normalize the order parameters to 1 when saturated (deep in phase).


[1] A. Vaswani, N. Shazeer, N. Parmar, J. Uszkoreit, L. Jones, A. N. Gomez, L. Kaiser, and I. Polosukhin, Attention is all you need, Adv. Neural Info. Proc. Syst. **30**, 6000 (2017).

[2] J. Kaplan, S. McCandlish, T. Henighan, T. B. Brown, B. Chess, R. Child, S. Gray, A. Radford, J. Wu, and D. Amodei, Scaling laws for neural language models, arXiv:2001.08361.

[3] T. B. Brown, B. Mann, N. Ryder, M. Subbiah, J. Kaplan, P. Dhariwal, A. Neelakantan, P. Shyam, G. Sastry, A. Askell, S. Agarwal, A. Herbert-Voss, G. Krueger, T. Henighan, R. Child, A. Ramesh, D. M. Ziegler, J. Wu, C. Winter, C. Hesse *et al.*, Language models are few-shot learners, Adv. Neural Info. Proc. Syst. **33**, 1877 (2020).

[4] P. Anderson, *Basic Notions Of Condensed Matter Physics*, 1st ed. (CRC Press, Boca Raton, FL, 1994).

[5] L. Balents, Spin liquids in frustrated magnets, Nature (London) **464**, 199 (2010).

[6] L. Savary and L. Balents, Quantum spin liquids: A review, Rep. Prog. Phys. **80**, 016502 (2017).

[7] C. Castelnovo, R. Moessner, and S. L. Sondhi, Magnetic monopoles in spin ice, Nature (London) **451**, 42 (2008).

[8] *Spin Ice*, Springer Series in Solid-State Sciences, Vol. 197, edited by L. Jaubert and M. Udagawa (Springer, Berlin, 2021).

[9] M. Hermele, M. P. A. Fisher, and L. Balents, Pyrochlore photons: The $U(1)$ spin liquid in a $S = 1/2$ three-dimensional frustrated magnet, Phys. Rev. B **69**, 064404 (2004).

[10] O. Benton, O. Sikora, and N. Shannon, Seeing the light: Experimental signatures of emergent electromagnetism in a quantum spin ice, Phys. Rev. B **86**, 075154 (2012).

[11] S. D. Pace, S. C. Morampudi, R. Moessner, and C. R. Laumann, Emergent fine structure constant of quantum spin ice is large, Phys. Rev. Lett. **127**, 117205 (2021).

[12] A. Kitaev, Anyons in an exactly solved model and beyond, Ann. Phys. **321**, 2 (2006).

[13] M. Hermanns, I. Kimchi, and J. Knolle, Physics of the kitaev model: Fractionalization, dynamic correlations, and material connections, Annu. Rev. Condens. Matter Phys. **9**, 17 (2018).

[14] N. Shannon, T. Momoi, and P. Sindzingre, Nematic order in square lattice frustrated ferromagnets, Phys. Rev. Lett. **96**, 027213 (2006).

[15] J. Carrasquilla and R. G. Melko, Machine learning phases of matter, Nat. Phys. **13**, 431 (2017).

[16] S. J. Wetzel, Unsupervised learning of phase transitions: From principal component analysis to variational autoencoders, Phys. Rev. E **96**, 022140 (2017).

[17] C. Wang and H. Zhai, Machine learning of frustrated classical spin models. I. Principal component analysis, Phys. Rev. B **96**, 144432 (2017).

[18] W. Hu, R. R. P. Singh, and R. T. Scalettar, Discovering phases, phase transitions, and crossovers through unsupervised machine learning: A critical examination, Phys. Rev. E **95**, 062122 (2017).

[19] S. J. Wetzel and M. Scherzer, Machine learning of explicit order parameters: From the Ising model to SU(2) lattice gauge theory, Phys. Rev. B **96**, 184410 (2017).

[20] M. J. S. Beach, A. Golubeva, and R. G. Melko, Machine learning vortices at the Kosterlitz-Thouless transition, Phys. Rev. B **97**, 045207 (2018).

[21] X. Liang, W.-Y. Liu, P.-Z. Lin, G.-C. Guo, Y.-S. Zhang, and L. He, Solving frustrated quantum many-particle models with convolutional neural networks, Phys. Rev. B **98**, 104426 (2018).

[22] C. Wang and H. Zhai, Machine learning of frustrated classical spin models (II): Kernel principal component analysis, Front. Phys. **13**, 130507 (2018).

[23] K. Liu, J. Greitemann, and L. Pollet, Learning multiple order parameters with interpretable machines, Phys. Rev. B **99**, 104410 (2019).

[24] J. Greitemann, K. Liu, L. D. C. Jaubert, H. Yan, N. Shannon, and L. Pollet, Identification of emergent constraints and hidden order in frustrated magnets using tensorial kernel methods of machine learning, Phys. Rev. B **100**, 174408 (2019).

[25] K.-W. Zhao, W.-H. Kao, K.-H. Wu, and Y.-J. Kao, Generation of ice states through deep reinforcement learning, Phys. Rev. E **99**, 062106 (2019).

[26] J. Greitemann, K. Liu, and L. Pollet, Probing hidden spin order with interpretable machine learning, Phys. Rev. B **99**, 060404 (2019).

[27] A. Decelle, V. Martin-Mayor, and B. Seoane, Learning a local symmetry with neural networks, Phys. Rev. E **100**, 050102 (2019).

[28] A. Canabarro, F. F. Fanchini, A. L. Malvezzi, R. Pereira, and R. Chaves, Unveiling phase transitions with machine learning, Phys. Rev. B **100**, 045129 (2019).

[29] B. Olsthoorn, J. Hellsvik, and A. V. Balatsky, Finding hidden order in spin models with persistent homology, Phys. Rev. Res. **2**, 043308 (2020).

[30] K. Liu, N. Sadoune, N. Rao, J. Greitemann, and L. Pollet, Revealing the phase diagram of Kitaev materials by machine learning: Cooperation and competition between spin liquids, Phys. Rev. Res. **3**, 023016 (2021).

[31] M. Doucet, A. M. Samarakoon, C. Do, W. T. Heller, R. Archibald, D. A. Tennant, T. Proffen, and G. E. Granroth, Machine learning for neutron scattering at ORNL*, Mach. Learn.: Sci. Technol. **2**, 023001 (2021).

[32] K. T. Butler, M. D. Le, J. Thiyagalingam, and T. G. Perring, Interpretable, calibrated neural networks for analysis and understanding of inelastic neutron scattering data, J. Phys.: Condens. Matter **33**, 194006 (2021).

[33] Z. Chen, N. Andrejevic, N. C. Drucker, T. Nguyen, R. P. Xian, T. Smidt, Y. Wang, R. Ernstorfer, D. A. Tennant, M. Chan, and M. Li, Machine learning on neutron and x-ray scattering and spectroscopies, Chem. Phys. Rev. **2**, 031301 (2021).

[34] S. Yu, Y. Gao, B.-B. Chen, and W. Li, Learning the effective spin Hamiltonian of a quantum magnet, Chin. Phys. Lett. **38**, 097502 (2021).

[35] A. M. Samarakoon, D. A. Tennant, F. Ye, Q. Zhang, and S. A. Grigera, Integration of machine learning with neutron scattering: Hamiltonian tuning in spin ice with pressure, arXiv:2110.15817.

[36] D. Lozano-Gómez, D. Pereira, and M. J. P. Gingras, Unsupervised machine learning of quenched gauge symmetries: A proof-of-concept demonstration, Phys. Rev. Res. **4**, 043118 (2022).

[37] A. M. Samarakoon, P. Laurell, C. Balz, A. Banerjee, P. Lampen-Kelley, D. Mandrus, S. E. Nagler, S. Okamoto, and D. A. Tennant, Extraction of interaction parameters for $\alpha$-$RuCl_3$ from neutron data using machine learning, Phys. Rev. Res. **4**, L022061 (2022).

[38] R. G. Melko and M. J. P. Gingras, Monte carlo studies of the dipolar spin ice model, J. Phys.: Condens. Matter **16**, R1277 (2004).

[39] L. D. C. Jaubert and P. C. W. Holdsworth, Signature of magnetic monopole and Dirac string dynamics in spin ice, Nat. Phys. **5**, 258 (2009).

[40] O. Cépas and B. Canals, Heterogeneous freezing in a geometrically frustrated spin model without disorder: Spontaneous generation of two time scales, Phys. Rev. B **86**, 024434 (2012).

[41] Y. Kato and S. Onoda, Numerical evidence of quantum melting of spin ice: Quantum-to-classical crossover, Phys. Rev. Lett. **115**, 077202 (2015).

[42] M. Udagawa, L. D. C. Jaubert, C. Castelnovo, and R. Moessner, Out-of-equilibrium dynamics and extended textures of topological defects in spin ice, Phys. Rev. B **94**, 104416 (2016).

[43] J. G. Rau and M. J. P. Gingras, Spin slush in an extended spin ice model, Nat. Commun. **7**, 12234 (2016).

[44] I. Nekrashevich, X. Ding, F. Balakirev, H. T. Yi, S.-W. Cheong, L. Civale, Y. Kamiya, and V. S. Zapf, Reaching the equilibrium state of the frustrated triangular Ising magnet $Ca_3Co_2O_6$, Phys. Rev. B **105**, 024426 (2022).

[45] Z. Fan and G.-W. Chern, Nonequilibrium generation of charge defects in kagome spin ice under slow cooling, Phys. Rev. E **109**, 054133 (2024).

[46] M. E. Zhitomirsky, Octupolar ordering of classical kagome antiferromagnets in two and three dimensions, Phys. Rev. B **78**, 094423 (2008).

[47] G.-W. Chern and R. Moessner, Dipolar order by disorder in the classical Heisenberg antiferromagnet on the kagome lattice, Phys. Rev. Lett. **110**, 077201 (2013).

[48] H. Takatsu, S. Onoda, S. Kittaka, A. Kasahara, Y. Kono, T. Sakakibara, Y. Kato, B. Fåk, J. Ollivier, J. W. Lynn, T. Taniguchi, M. Wakita, and H. Kadowaki, Quadrupole order in the frustrated pyrochlore $Tb_{2+x}Ti_{2-x}O_{7+y}$, Phys. Rev. Lett. **116**, 217201 (2016).

[49] M. Taillefumier, O. Benton, H. Yan, L. D. C. Jaubert, and N. Shannon, Competing spin liquids and hidden spin-nematic order in spin ice with frustrated transverse exchange, Phys. Rev. X **7**, 041057 (2017).

[50] A. Hemmatzade, K. Essafi, M. Taillefumier, M. Müller, T. Fennell, and P. M. Derlet, Fluctuation-induced spin nematic order in magnetic charge ice, Phys. Rev. B **109**, 224423 (2024).

[51] X. Ran, Z. Yan, Y.-C. Wang, R. Samajdar, J. Rong, S. Sachdev, Y. Qi, and Z. Y. Meng, Hidden orders and phase transitions for the fully packed quantum loop model on the triangular lattice, Commun. Phys. **7**, 207 (2024).

[52] A. Szabo, S. A. Grigera, P. C. W. Holdsworth, L. D. C. Jaubert, R. Moessner, D. G. Slobinsky, M. Sturla, and R. A. Borzi, Perfectly hidden order and Z2 confinement transition in a fully packed monopole liquid, arXiv:2406.09336.

[53] H. Yan, O. Benton, L. D. C. Jaubert, and N. Shannon, Rank–2 $U(1)$ spin liquid on the breathing pyrochlore lattice, Phys. Rev. Lett. **124**, 127203 (2020).

[54] S. Han, A. S. Patri, and Y. B. Kim, Realization of fractonic quantum phases in the breathing pyrochlore lattice, Phys. Rev. B **105**, 235120 (2022).

[55] E. Z. Zhang, F. L. Buessen, and Y. B. Kim, Dynamical signatures of rank-2 $U(1)$ spin liquids, Phys. Rev. B **105**, L060408 (2022).

[56] M. Pretko, Generalized electromagnetism of subdimensional particles: A spin liquid story, Phys. Rev. B **96**, 035119 (2017).

[57] A. Prem, S. Vijay, Y.-Z. Chou, M. Pretko, and R. M. Nandkishore, Pinch point singularities of tensor spin liquids, Phys. Rev. B **98**, 165140 (2018).

[58] A. Rasmussen, Y.-Z. You, and C. Xu, Stable gapless Bose liquid phases without any symmetry, arXiv:1601.08235.

[59] J. Haah, Local stabilizer codes in three dimensions without string logical operators, Phys. Rev. A **83**, 042330 (2011).

[60] C. T. Aitchison, D. Bulmash, A. Dua, A. C. Doherty, and D. J. Williamson, Boundaries and defects in the cubic code, Phys. Rev. B **109**, 205125 (2024).

[61] C. Xu, Gapless bosonic excitation without symmetry breaking: An algebraic spin liquid with soft gravitons, Phys. Rev. B **74**, 224433 (2006).

[62] M. Pretko, Emergent gravity of fractons: Mach's principle revisited, Phys. Rev. D **96**, 024051 (2017).

[63] H. Yan, Hyperbolic fracton model, subsystem symmetry, and holography, Phys. Rev. B **99**, 155126 (2019).

[64] H. Yan, Hyperbolic fracton model, subsystem symmetry, and holography. II. The dual eight-vertex model, Phys. Rev. B **100**, 245138 (2019).

[65] H. Yan, Geodesic string condensation from symmetric tensor gauge theory: A unifying framework of holographic toy models, Phys. Rev. B **102**, 161119 (2020).

[66] H. Yan, C. B. Jepsen, and Y. Oz, $p$-adic holography from the hyperbolic fracton model, arXiv:2306.07203.

[67] T. Haku, K. Kimura, Y. Matsumoto, M. Soda, M. Sera, D. Yu, R. A. Mole, T. Takeuchi, S. Nakatsuji, Y. Kono, T. Sakakibara, L.-J. Chang, and T. Masuda, Low-energy excitations and ground-state selection in the quantum breathing pyrochlore antiferromagnet $Ba_3Yb_2Zn_5O_{11}$, Phys. Rev. B **93**, 220407 (2016).

[68] J. G. Rau, L. S. Wu, A. F. May, L. Poudel, B. Winn, V. O. Garlea, A. Huq, P. Whitfield, A. E. Taylor, M. D. Lumsden, M. J. P. Gingras, and A. D. Christianson, Anisotropic exchange within decoupled tetrahedra in the quantum breathing pyrochlore $Ba_3Yb_2zn_5O_{11}$, Phys. Rev. Lett. **116**, 257204 (2016).

[69] L. E. Chern, Y. B. Kim, and C. Castelnovo, Competing quantum spin liquids, gauge fluctuations, and anisotropic interactions in a breathing pyrochlore lattice, Phys. Rev. B **106**, 134402 (2022).

[70] B. Canals, M. Elhajal, and C. Lacroix, Ising-like order by disorder in the pyrochlore antiferromagnet with dzyaloshinskii-moriya interactions, Phys. Rev. B **78**, 214431 (2008).

[71] G.-W. Chern, Pyrochlore antiferromagnet with antisymmetric exchange interactions: Critical behavior and order from disorder, arXiv:1008.3038.

[72] V. Noculak, D. Lozano-Gomez, J. Oitmaa, R. R. P. Singh, Y. Iqbal, M. J. P. Gingras, and J. Reuther, Classical and quantum phases of the pyrochlore $S = 1/2$ magnet with Heisenberg and Dzyaloshinskii-Moriya interactions, Phys. Rev. B **107**, 214414 (2023).

[73] R. Moessner and J. T. Chalker, Properties of a classical spin liquid: The Heisenberg pyrochlore antiferromagnet, Phys. Rev. Lett. **80**, 2929 (1998).

[74] R. Moessner and J. T. Chalker, Low-temperature properties of classical geometrically frustrated antiferromagnets, Phys. Rev. B **58**, 12049 (1998).

[75] S. V. Isakov, K. Gregor, R. Moessner, and S. L. Sondhi, Dipolar spin correlations in classical pyrochlore magnets, Phys. Rev. Lett. **93**, 167204 (2004).

[76] C. L. Henley, Power-law spin correlations in pyrochlore antiferromagnets, Phys. Rev. B **71**, 014424 (2005).

[77] C. L. Henley, The "coulomb phase" in frustrated systems, Annu. Rev. Condens. Matter Phys. **1**, 179 (2010).

[78] O. Benton, L. D. C. Jaubert, H. Yan, and N. Shannon, A spin liquid with pinch-line singularities on the pyrochlore lattice, Nat. Commun. **7**, 11572 (2016).

[79] O. Benton, Classical and quantum spin liquids on the pyrochlore lattice, Ph.D. thesis, University of Bristol, 2014.

[80] H. Yan, O. Benton, R. Moessner, and A. H. Nevidomskyy, Classification of classical spin liquids: Typology and resulting landscape, Phys. Rev. B **110**, L020402 (2024).

[81] H. Yan, O. Benton, A. H. Nevidomskyy, and R. Moessner, Classification of classical spin liquids: Detailed formalism and suite of examples, Phys. Rev. B **109**, 174421 (2024).

[82] M. Pretko, X. Chen, and Y. You, Fracton phases of matter, Int. J. Mod. Phys. A **35**, 2030003 (2020).

[83] M. Pretko, Subdimensional particle structure of higher rank $U(1)$ spin liquids, Phys. Rev. B **95**, 115139 (2017).

[84] H. Yan, O. Benton, L. Jaubert, and N. Shannon, Theory of multiple-phase competition in pyrochlore magnets with anisotropic exchange with application to $Yb_2Ti_2O_7$, $Er_2Ti_2O_7$, and $Er_2Sn_2O_7$, Phys. Rev. B **95**, 094422 (2017).

[85] R. M. Nandkishore and M. Hermele, Fractons, Annu. Rev. Condens. Matter Phys. **10**, 295 (2019).

[86] A. Gromov and L. Radzihovsky, *Colloquium*: Fracton matter, Rev. Mod. Phys. **96**, 011001 (2024).

[87] P. Mendels and A. Wills, Kagome antiferromagnets: Materials vs spin liquid behaviors, in *Introduction to Frustrated Magnetism*, Solid State Science, Vol. 164, edited by C. Lacroix, P. Mendels, and F. Mila (Springer, Berlin, 2011).

[88] P. de Gennes and J. Prost, *The Physics of Liquid Crystals*, International Series of Monographs on Physics (Clarendon, Oxford, 1995).

[89] N. Shannon, K. Penc, and Y. Motome, Nematic, vector-multipole, and plateau-liquid states in the classical $O(3)$ pyrochlore antiferromagnet with biquadratic interactions in applied magnetic field, Phys. Rev. B **81**, 184409 (2010).

[90] B. Javanparast, Z. Hao, M. Enjalran, and M. J. P. Gingras, Fluctuation-driven selection at criticality in a frustrated magnetic system: The case of multiple-**k** partial order on the pyrochlore lattice, Phys. Rev. Lett. **114**, 130601 (2015).

[91] P. G. Welch, J. A. M. Paddison, M. D. Le, J. S. Gardner, W.-T. Chen, A. R. Wildes, A. L. Goodwin, and J. R. Stewart, Magnetic structure and exchange interactions in the Heisenberg pyrochlore antiferromagnet $Gd_2Pt_2O_7$, Phys. Rev. B **105**, 094402 (2022).

[92] J. A. M. Paddison, L. Yin, K. M. Taddei, M. J. Cochran, S. Calder, D. S. Parker, and A. F. May, Multiple incommensurate magnetic states in the kagome antiferromagnet $Na_2Mn_3Cl_8$, Phys. Rev. B **108**, 054423 (2023).

[93] S. E. Palmer and J. T. Chalker, Order induced by dipolar interactions in a geometrically frustrated antiferromagnet, Phys. Rev. B **62**, 488 (2000).

[94] P. A. McClarty, P. Stasiak, and M. J. P. Gingras, Order-by-disorder in the $xy$ pyrochlore antiferromagnet, Phys. Rev. B **89**, 024425 (2014).

[95] J. G. Rau, E. K.-H. Lee, and H.-Y. Kee, Generic spin model for the honeycomb iridates beyond the Kitaev limit, Phys. Rev. Lett. **112**, 077204 (2014).

[96] L. Janssen and M. Vojta, Heisenberg–Kitaev physics in magnetic fields, J. Phys.: Condens. Matter **31**, 423002 (2019).

[97] N. Rao, K. Liu, M. Machaczek, and L. Pollet, Machine-learned phase diagrams of generalized Kitaev honeycomb magnets, Phys. Rev. Res. **3**, 033223 (2021).

[98] N. Sadoune, G. Giudici, K. Liu, and L. Pollet, Unsupervised interpretable learning of phases from many-qubit systems, Phys. Rev. Res. **5**, 013082 (2023).

[99] K. A. Ross, L. Savary, B. D. Gaulin, and L. Balents, Quantum excitations in quantum spin ice, Phys. Rev. X **1**, 021002 (2011).

[100] V. N. Kotov, M. Elhajal, M. E. Zhitomirsky, and F. Mila, Dzyaloshinsky-Moriya-induced order in the spin-liquid phase of the $S = 1/2$ pyrochlore antiferromagnet, Phys. Rev. B **72**, 014421 (2005).